Nonlithostatic pressure during subduction and collision and the formation of (ultra)high-pressure rocks
Georg Reuber et al.

# NON-LITHOSTATIC PRESSURES DURING SUBDUCTION AND COLLISION – SUPPLEMENTARY MATERIAL

Here, we first describe the numerical method we use along with a discussion on the employed rheologies and the use of plastic friction angle in many geodynamic models (part S1). In a subsequent section (S2) we describe the model setup and compare results of our finite element code with the earlier results of Li et al. (2010) obtained with a staggered finite difference method. We than describe the effect of adding an inclusion in the reference model in more detail (S3), followed by a summary of the systematic results (S4) and a discussion of the effect of elasticity on the conclusions.

## S1. Method

The simulations described in this paper are computed with the thermo-mechanical marker-and-cell finite-element code, MVEP2 (Thielmann and Kaus, 2012; Johnson et al., 2014) that simulates deformation of the lithosphere and mantle in the presence of a free surface for temperature-dependent viscoelastoplastic rock rheologies.

### *Governing equations*

The conservation of mass and the momentum for slowly deforming incompressible rocks are

$$\frac{\partial v_i}{\partial x_i} = 0 \quad (1)$$

$$-\frac{\partial P}{\partial x_i} + \frac{\partial \tau_{ij}}{\partial x_j} = \rho g_i \quad (2)$$

where $v_i$ denotes velocity, $P$ pressure, $\tau_{ij}$ the components of the deviatoric stress tensor, $g_i$ gravitational acceleration and $\rho$ density. Density is assumed to be temperature-dependent according to:

$$\rho = \rho_0\big(1 - \alpha(T - T_0)\big) \tag{3}$$

where $\alpha$ is the thermal expansion coefficient, and $\rho_0$the density at room temperature $T_0$.

We employ a Maxwell visco-elasto-plastic rheology

$$\dot{\varepsilon}_{ij} = \dot{\varepsilon}_{ij}^{elastic} + \dot{\varepsilon}_{ij}^{viscous} + \dot{\varepsilon}_{ij}^{plastic} = \frac{1}{2G}\frac{D\tau_{ij}}{Dt} + \frac{\tau_{ij}}{2\eta_{\text{eff}}} + \dot{\lambda}\frac{\partial Q}{\partial \sigma_{ij}} \tag{4}$$

where $\dot{\varepsilon}_{ij}$ are the components of the strain rate tensor, $G$ the elastic shear modulus, $\frac{D\tau_{ij}}{Dt}$ Jaumann objective derivative of the deviatoric stress tensor (Thielmann et al., 2015), $\eta_{\text{eff}}$ the effective viscosity which generally depends on stress and temperature, $\dot{\lambda}$ a plastic multiplyer that ensures that stresses are below or at the yield stress, $Q$ the plastic flow potential and $\sigma_{ij} = -P\delta_{ij} + \tau_{ij}$ the components of the stress tensor with $\delta_{ij}$ being the Kronecker delta. Most simulations presented here do not take elasticity into account for consistency with the earlier results of Li et al. (2010), which is achieved by setting G to a very large value ($10^{60}$ Pa). Yet, we did test the effect of elasticity on our general conclusions which shows that it does not significantly change the results (section S5). In addition, we also solve the energy equation which is given by

$$\rho c_p\left(\frac{\partial T}{\partial t} + v_i\frac{\partial T}{\partial x_i}\right) = \frac{\partial}{\partial x_i}\left(k\frac{\partial T}{\partial x_i}\right) + H_a + H_r + H_s \tag{5}$$

where $c_p$ is the heat capacity, $k$ the thermal conductivity, $H_r$ radioactive heating, $H_s = \tau_{ij}\big(\dot{\varepsilon}_{ij} - \dot{\varepsilon}_{ij}^{elastic}\big)$ shear heating caused by dissipative processes, and $H_a = -T\alpha\rho g_z v_z$ adiabatic heating.

***Viscosity***

The effective viscosity is computed according to

$$\eta_{\text{eff}} = FA^{-1/n}(\dot{\varepsilon}_{II})^{\frac{1-n}{n}}\exp\left(\frac{E+PV}{nRT}\right) \quad (6)$$

where $n$ is a powerlaw exponent, $E$ the activation energy, $V$ the activation volume, $\dot{\varepsilon}_{II} = \left(0.5\dot{\varepsilon}_{ij}\dot{\varepsilon}_{ij}\right)^{0.5}$ the second invariant of the strain rate tensor, $R$ the universal gas constant, $F$ a coefficient that depends on whether the experiment was done for uniaxial or simple shear conditions (Gerya, 2009), and $A$ an experimentally determined pre-factor. Values are taken from laboratory experiments and are listed in Table S2.

In all simulations in this paper, a viscosity cutoff of $10^{25}$ Pas and $10^{19}$ Pas is employed.

***Plasticity***

The maximum stress of rocks is limited, and in the crust, this maximum yield stress is pressure dependent according to Byerlees law. The usual way in which this is modelled in geodynamic codes is by imposing a Mohr-Coulomb or Drucker-Prager yield criterium which is given by

$$\sigma_{yield} = C + \mu\left(P - P_f\right) \quad (7)$$

where $C$ is the rock cohesion, $P$ dynamic pressure, $P_f$ fluid pressure and $\mu$ the coefficient of friction . Byerlees law, based on experiments, suggests that $\mu$ is 0.85 for pressures smaller than 200 MPa and $\mu = 0.6$ for pressures larger than that (Byerlee, 1978). In-situ stress measurements in (deep) drill holes in the upper crust suggest that $\mu$ varies between 0.6 and 1.0 with the upper values being applicable for the uppermost crust (Townend and Zoback, 2000). The San Andreas Fault Observatory at Depth (SAFOD) drill-hole gave an opportunity to measure the plastic strength of rocks just outside and within the San Andreas Fault zone, which showed that $\mu$ is around 0.6 outside the fault and reduced to 0.15 on the actual fault itself (Lockner et al., 2011), which suggests that Byerlees law is valid as a general first-order approximation of the yield stress of the overall crust, outside major fault zones which have smaller values. Often, the yield stress is expressed in terms of a friction angle rather than a friction coefficient, where $\mu = \tan(\phi)$. With that, equation (7) can be rewritten as

$$\sigma_{yield} = C + \left(P - P_f\right)\tan(\phi) \tag{8}$$

At yielding, the radius of the Mohr-circle touches the yield strength envelope. The radius of the Mohr circle is given by the second invariant of the (deviatoric) stress tensor, $\tau_{II} = \left(0.5\tau_{ij}\tau_{ij}\right)^{0.5}$. This gives the following trigonometric expression

$$\sin(\phi) = \frac{\tau_{II}}{\frac{C}{\tan(\phi)} + \left(P - P_f\right)}$$

which can be written as

$$\tau_{II} = C\cos(\phi) + \left(P - P_f\right)\sin(\phi)$$

Stresses in the model should be smaller or equal to this yield stress

$$\tau_{II} \leq C\cos(\phi) + \left(P - P_f\right)\sin(\phi) \tag{9}$$

This can again be rewritten as

$$\tau_{II} \leq C\cos(\phi) + P\lambda\sin(\phi) \tag{10}$$

where $\lambda = \left(1 - \frac{P}{P_f}\right)$ is a factor that depends on how high the fluid pressure is. If there are no fluids, $P_f = 0$ and $\lambda = 1$. If, on the other hand, fluid is present in small unconnected pores within the rock, the fluid pressure might reach $P$ and $\lambda = 0$. If fluid pressure is present in an interconnected network that reaches to the Earth surface, the fluid pressure is close to hydrostatic, and $P_f = \rho_f g z$, where $\rho_f$ is the *fluid* density (around 1000 kg/m$^3$ for water) and $z$

the depth. If the rock pressure is lithostatic, $P = \rho g z$, which gives, using a rock density of 3000 kg/m$^3$, $\lambda = \frac{2}{3} = 0.67$. If, however, rock pressure is twice larger than lithostatic and fluid pressure remains hydrostatic we obtain $\lambda = \frac{5}{6} = 0.83$.

Some authors use an *effective* friction angle $\phi_{\text{eff}}$ rather than the true friction angle $\phi$ and a pore-fluid factor $\lambda$. This can be derived by stating that

$$\sin(\phi_{\text{eff}}) = \lambda \sin(\phi)$$

in that case we can reformulate equation (10) as

$$\tau_{II} \leq C\cos(\phi) + P\sin(\phi_{\text{eff}}) \tag{11}$$

With $\phi_{\text{eff}} = \text{asin}\,(\lambda \sin(\phi))$. This derivation shows that even if we use an effective friction angle in the yield stress, we also need to take the "dry" friction angle $\phi$ into account. Some authors simply replace the friction angle in their model $\phi_{\text{eff}}$ with a smaller value $\phi_{\text{eff}}$ and justify this with elevated fluid pressures. The yield stress criterion they solve in that case is:

$$\tau_{II} \leq C\cos(\phi_{\text{eff}}) + P\sin(\phi_{\text{eff}})$$

which is only correct if the cohesion is zero (which it often is not). Whereas it might be argued that cohesion is a small term in the expression above, this discussion does show that it is actually better to incorporate equation (10) directly in the numerical code rather than using small friction angle values.

As discussed, experimental evidence in rocks from the SAFOD experiment shows that $\mu = 0.6$ ($\phi = 31°$) in the crust (also just outside the large fault zone), and is only reduced to smaller values of $\mu = 0.15$ ($\phi = 8.5°$) within the actively deforming fault zones. If one wishes to correctly model the long-term averaged state of stress in the crust, it is thus probably best to use a "dry" coefficient of friction for crustal rocks, and weaken this within fault zones only.

Models of subduction dynamics and collision generally use a rather small friction angle within the subduction channel to prevent unrealistically high topographies and slab breakoff to develop, an effect which we also find in our simulations. Using a low friction angle for sedimentary rocks at the ocean floor seems indeed justified to a certain extent as (unconsolidated) sediments on the ocean floor are water rich and might develop high fluid pressures at larger depth.

Another recent argument is that melt propagation in dikes results in short bursts of weakness of the lithosphere. The long-term mechanical behavior of the lithosphere, and the dissipation of its mechanical energy, was shown to strongly correlate to the energy that is dissipated during rapid magmatic diking events, which was shown to result in values of $\lambda$ of $10^{-4}$-$10^{-2}$ (Gerya et al., 2015). Whereas we agree that the mechanical deformation of the lithosphere might be controlled by the small period's weakness, using very small values of $\lambda$ will result in small stresses (and pressures) throughout the whole simulation. Metamorphic reactions require time and as such they are more likely controlled by the larger stresses that exist during amagmatic periods, rather than by what happens during a rapid magmatic event, and we would therefore argue for using the dry friction values throughout most of the crust and employing small values only on strongly weakened fault zones.

From the yield stress expression (eq. (10)), one can compute an effective plastic viscosity:

$$\eta_{pl} = \frac{C\cos(\phi) + P\lambda\sin(\phi)}{2\dot{\varepsilon}_{II}} \tag{12}$$

The effective plastic viscosity is then adapted such that stresses remain at or below yield stresses, which require nonlinear iterations (Kaus, 2010). In our code we employ fixed-point iterations to deal with those.

***Erosion and sedimentation***

The free surface $h_{\mathrm{topo}}$ evolves according to:

$$\frac{\partial h_{\text{topo}}}{\partial t} + v_x \frac{\partial h_{\text{topo}}}{\partial x} + v_z \frac{\partial h_{\text{topo}}}{\partial z} = v_s + v_{er}$$

where $v_s$ is the sedimentation rate which is 1 mm/yr if $h_{\text{topo}} < 100$m, and $v_e$ is the erosion rate which is -3 mm/yr if $h_{\text{topo}} > 4000$m. The free surface is remeshed to the new grid location at every time step, using the x-coordinates of the finite element mesh.

***Numerical method***

Our numerical equations (1-6) and (11) are solved numerically using the MATLAB-based finite element method MVEP2, which is a further-development of MILAMIN_VEP (Kaus, 2010; Thielmann and Kaus, 2012) that uses markers to track material properties, and creates a new topography-following mesh at every time step. As most other geodynamic codes, we use pressure, velocity and temperature as primary variables. For most simulations reported here, we employ $Q_1P_0$ elements with direct solvers. We performed a few tests with higher order $Q_2P_{-1}$ elements and found the first-order effects such as geometry, magnitude and distribution of pressures to be the same, even though the peak pressures are slightly larger for $Q_2P_{-1}$ elements (on the order of ~100 MPa in the strong inclusion case of Figure 1).

***Non-lithostatic pressure***

Pressure is defined as the negative trace of the stress tensor and is one of our solution variables, and since we use a free surface upper boundary condition it is uniquely defined in our simulations. In order to compare this with the lithostatic pressure we need a method to compute the equivalent lithostatic pressure everywhere in our model. Technically, it can be derived from the force balance equation (eq. (2)) under the assumption that deviatoric stresses are zero, which gives:

$$-\frac{\partial P_L}{\partial z} = \rho g \qquad (13)$$

In the case that density is constant and gravity acts in the negative vertical direction and is zero at the Earth's surface, we can solve this analytically:

$$P_L = \rho g h$$

where $h$ is depth. Yet, in our models density actually depends on phase and temperature. Moreover, we use a deformed finite element mesh where density values are only evaluated at integration points. In order to compute lithostatic pressure in that case, we could interpolate density values on a regular grid and integrate the pressure numerically, starting at the surface. Yet, this gives rise to interpolation errors. A better method is to discretize equation (13) with a finite element method and employ the same shape functions and deformed elements as we use in the thermomechanical code. This requires a boundary condition, which is that $P_L = 0$ at the surface. We implemented this method which compares well with the normal integration method but is more consistent with the overall code. Once this is computed, the non-lithostatic pressure can be evaluated with

$$P_T = P - P_L \qquad (14)$$

***Tracking P-T evolution of rocks***

In order to create plots of the maximum pressure that a particle experienced during its model evolution, one could store all particles during the full model evolution. Yet, in practice this requires immense storage volumes, particularly if several hundred simulations are performed. We therefore use a different technique, which traces particles backwards in time though the model using a 4$^{th}$ order Runga-Kutta method in time, which uses stored velocity fields. We compared this method with simulations in which the full particle fields were stored and found that this method yielded nearly identical results provided that sufficient intermediate velocity fields are stored. We used this method to create plots of the maximum pressure that a marker experienced during its model evolution in figure 1.

The PT-paths shown in figure 1 were computed from a single marker, but we compared the results with a case in which 50 markers were used and found the results to be similar.

The quartz/coesite phase transition was calculated using THERMOCALC v3.62 and the Holland & Powell (2011) database.

***Rheology parameters employed***

A summary of all rheology parameters employed in the models is given in Table S1. Parameters are taken from (Shelton and Tullis, 1981; Kirby, 1983; Ranalli and Murphy, 1987; Wilks and Carter, 1990; Bittner and Schmeling, 1995; Ranalli, 1995; Mackwell and Zimmerman, 1998; Turcotte and Schubert, 2002).

## S2. Model setup and reproducing earlier results

### *Model setup*

Unlike the study of Li et al. (2010), which employed a marker and cell finite difference method (Gerya and Yuen, 2007), we use an independently developed thermo-mechanical finite element code (MVEP2; see supplementary material and (Thielmann and Kaus, 2012; Johnson et al., 2014) for details). The initial model setup has two continents, each with a 2 km sedimentary cover layer, a 15.5 km thick quartzitic upper and a 17.5 km thick plagioclase lower crust (Figure S1a; see table S1 for all employed model parameters). Subduction is initiated by imposing a constant convergence velocity of 3 cm/a for the rightmost lithosphere together with an initial weak zone. The initial geotherm increases linearly from 0°C at the surface to 1350°C at 150 km depth (i.e., 9°C/km), after which it increases adiabatically to 1605°C at the isothermal lower boundary. The side and lower boundaries are free slip whereas the upper boundary is stress free, which is slightly different than the models of (Li et al., 2010) who use an "infinite-like" lower boundary together with a sticky air layer to simulate water and air (see Fig. S1a for the model setup). The upper boundary is subjected to a constant erosion rate of 3 mm/a when the elevation is higher than 4 km and to a constant sedimentation rate of 1 mm/a for areas below 100 meters (Li et al. 2010 did not specify an erosion/sedimentation rate but from their figures it appears that erosion was active). We employ ~7 million markers to track composition and temperature and employ quadrilateral finite elements with a resolution that varies from 30x30 km at the lateral boundaries to 2x2 km around the subduction zone. The rheology we employ uses laboratory-derived creep laws for viscous rocks combined with a frictional plastic (pressure-dependent) yield stress (see Fig. S1b for a strength-envelop representation of the rheology used in our models, for a constant background strain rate of $10^{-15}$ $s^{-1}$). Our model parameters closely follow those used by (Li et al., 2010) (see supplementary tables 1), but are not identical. We, for example, use a constant rather than a temperature dependent thermal conductivity and ignore melting and crystallization.

The reference simulation has a laterally homogeneous crust with a plastic friction angle of 7$^o$, to reflect high fluid pressures in the crust. This value is considerably smaller than the ~40$^o$ determined experimentally (Byerlee, 1978) and ~30$^o$ by in-situ stress measurements in boreholes (Townend and Zoback, 2000).

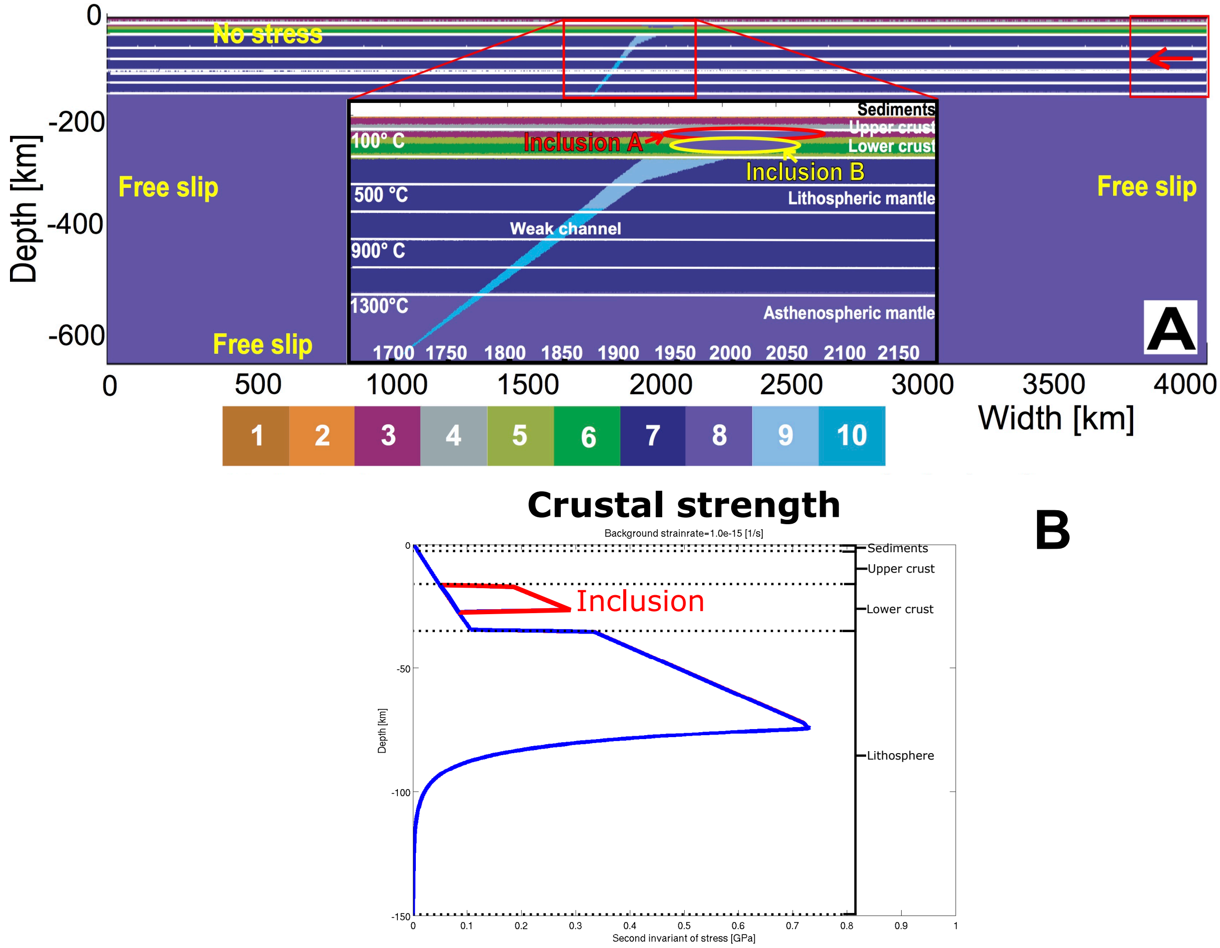


**Figure S1 | Model setup and strength for the simulations shown here:** A) The model setup consists of two continents separated by a weak zone, where colors indicate: [1,2]Sediments; [3,4]Upper crust; [5,6]Lower crust; [7]Lithospheric mantle; [8]Asthenospheric mantle; [9]Upper weak zone; [10]Lower weak zone. The lithosphere is pushed from the right with a constant velocity within the red box. B) Strength envelop for the model setup we employed under a constant, pure shear, background strain rate of $10^{-15}$ $s^{-1}$ (note that strain rates, and therefore stresses, in the 2D simulations vary significantly).

### *Reproducing earlier results*

The simulation results in subduction initiation, followed by formation of a subduction channel, burial and exhumation of upper crustal rocks and subduction of lower crustal rocks. The overall geometry and thermal evolution of our model is very similar to the previously published results, apart from small-scale features within the upper crust and subduction wedge (Figure S2). Plots of the non-lithostatic pressure component during various model stages are similar as well, and show that pressures within the strong mantle lithosphere can strongly deviate from lithostatic (supplementary Figure S3 and S4). In both models, pressures within the subduction channel, from which rocks are exhumed at later stages, remain close to lithostatic suggesting that petrological pressure estimates can be directly transferred into depth for low effective friction angles.

Overall, the results agree, but there are some differences in the numerical approach. First, we used a free slip lower boundary condition, rather than an 'infinite' like lower boundary, which might be the major reason why Li et al. (2010) have a change in slab polarity in the middle of the simulation, which our results do not show. Also, it was not possible to obtain the exact same number of particles or the geometry of the subduction channel. We did not implement the phase transition to molten material and do not set a 'water' phase if topography is below zero, which might be the reason for the different material circulation within the sediment phase. Given that we use completely independently developed codes and even different numerical techniques, we can reproduce their results reasonably well particularly with respect to the shape of the subduction channel and the maximum non-lithostatic pressure values reached. Differences in the deformation patterns in the crust are expected as such fine scale features are not resolved with the model resolution employed here.

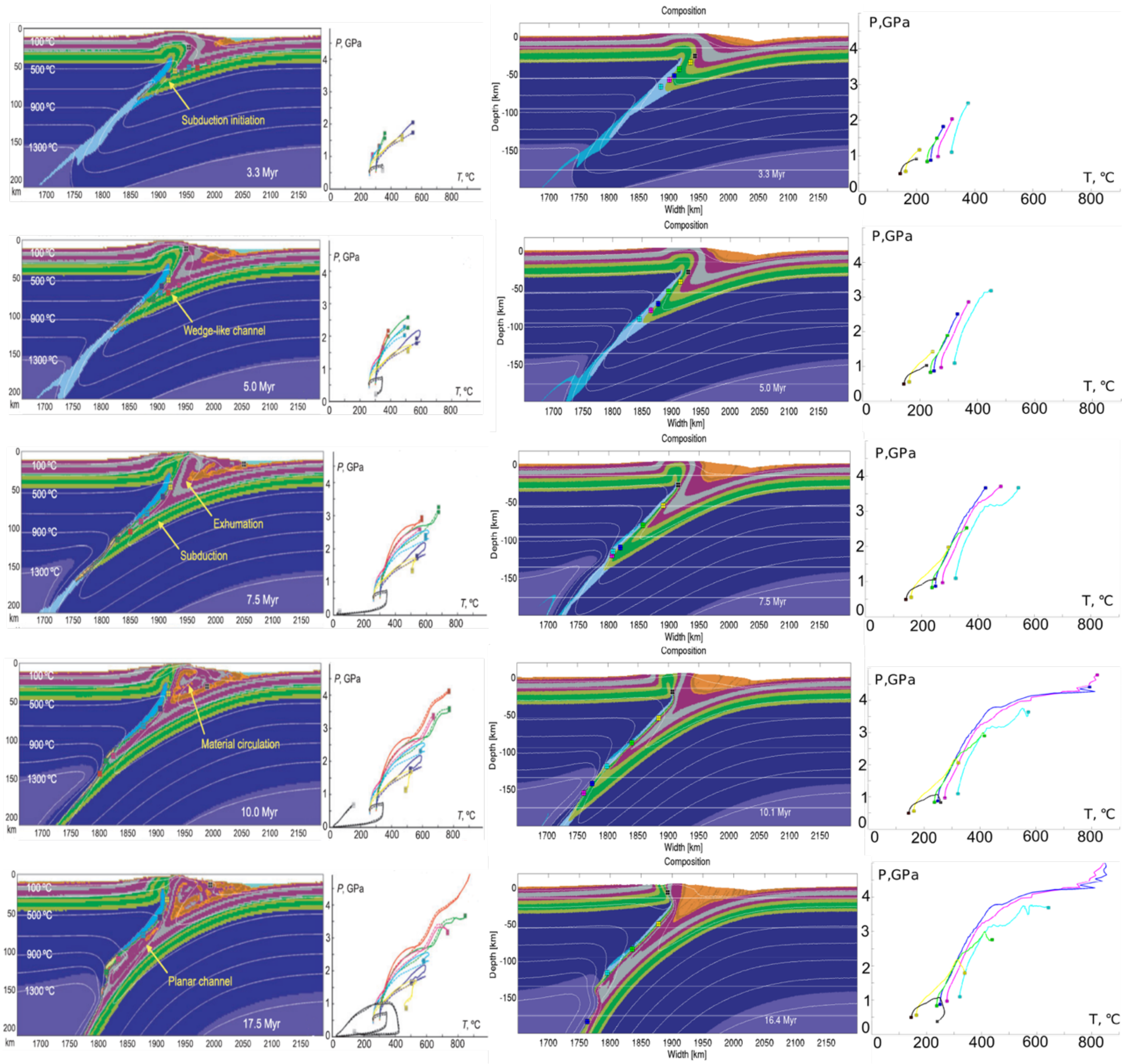


**Figure S2 | Comparison of I2VIS vs MVEP2.** Left column: Original pictures by Li et al. (2010) showing the evolution of their reference model. The P-T paths show the pressure-temperature history of the highlighted markers. Right column: Our reproduction of their reference model, using a different numerical code (MVEP2), and slightly different lower boundary conditions (free slip rather than an infinitely-like boundary condition). The markers for the P-T paths have slightly different locations than the ones in Li et al. (2010).

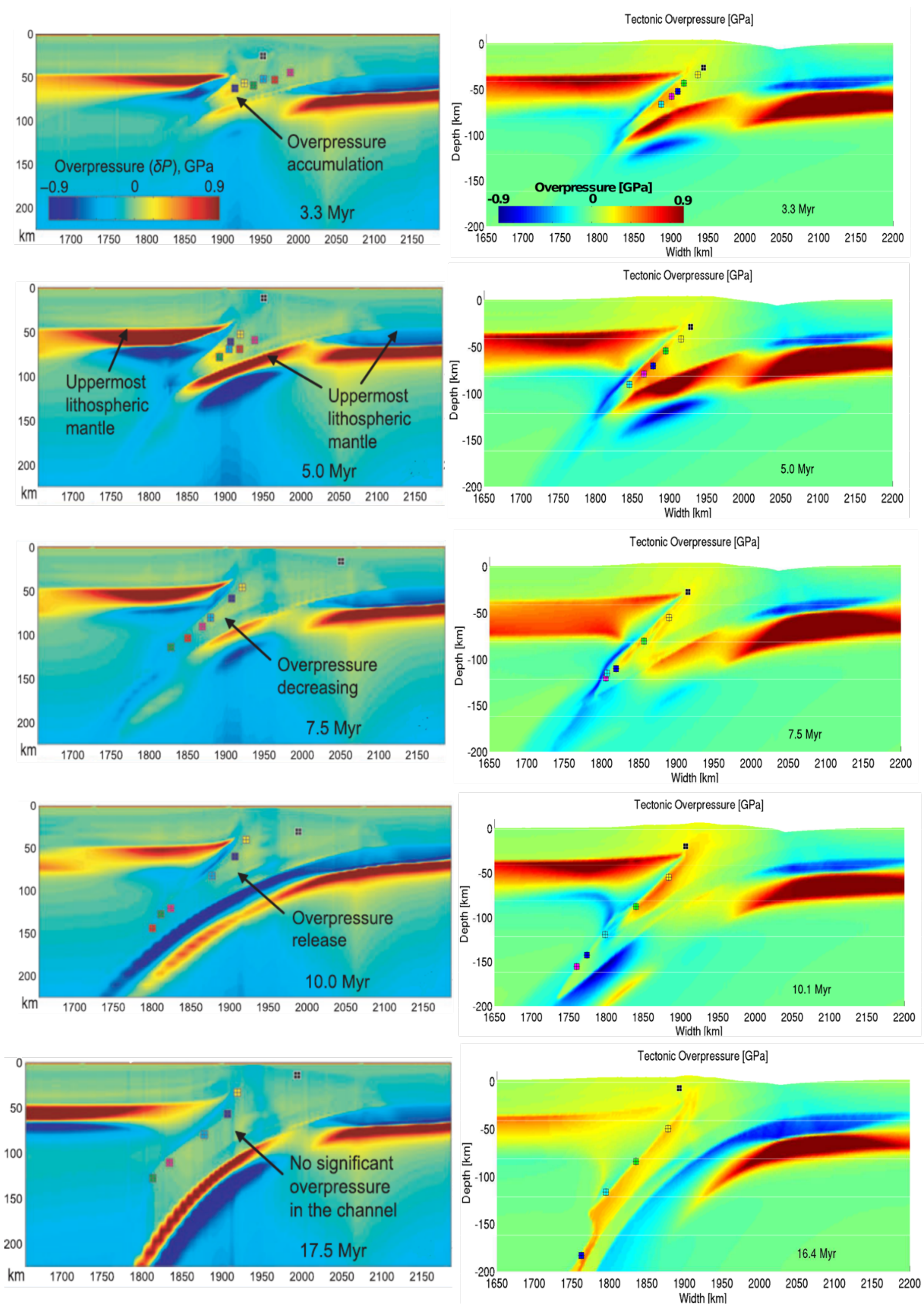


**Figure S3. Non-lithostatic pressure, I2VIS vs. MVEP2.** Left column: Original pictures taken from Li et al. (2010) showing the non-lithostatic pressure in GPa. Right column: Our reproduction of the non-lithostatic pressure in their reference model also in GPa.

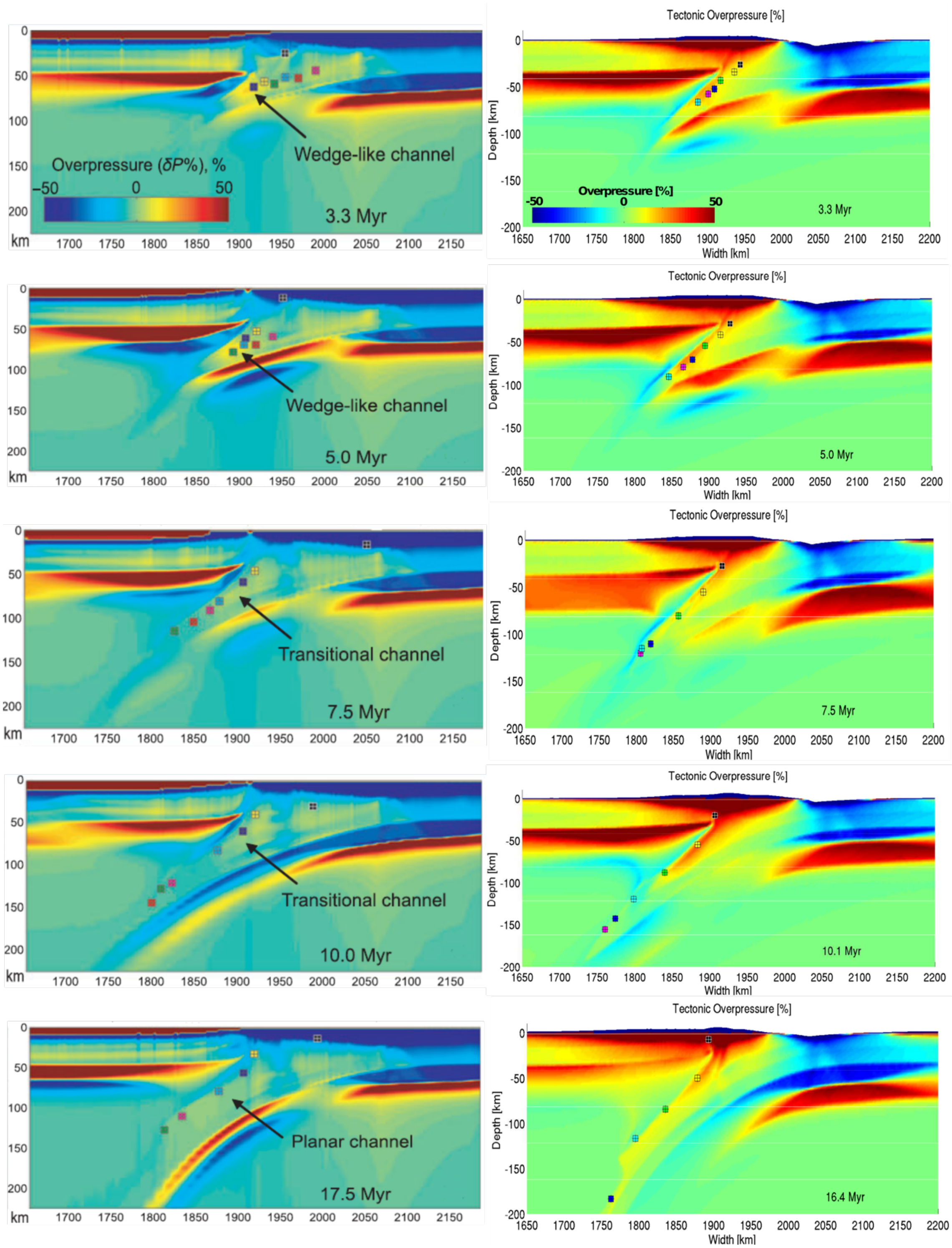


**Figure S4. Relative non-lithostatic pressure, I2VIS vs. MVEP2.** Left column: Original pictures taken from Li et al. (2010) showing the non-lithostatic pressure as percentage of the lithostatic pressure. Right column: Our reproduction of the non-lithostatic pressure in their reference model also as percentage of the lithostatic pressure

## S3. Effect of heterogeneity

In order to test the effect of heterogeneities, we emplaced a heterogeneity of type ”A” (Fig. S1) at the upper/lower crust boundary which is otherwise identical to the one described earlier. The heterogeneity has a thickness of 10 km and a width of 150 km, which is larger than typical crustal heterogeneities but ensures that it is computationally well-resolved. Results show that the presence of the heterogeneity affects the deformation and exhumation patterns within the upper crust and mountain belt, but does not have a major impact on the overall subduction dynamics (Figure S5a). Yet, the maximum recorded pressures during the lifetime of the heterogeneity are significantly larger than lithostatic (Figure S5b), which can be attributed to compression and bending of the layer.

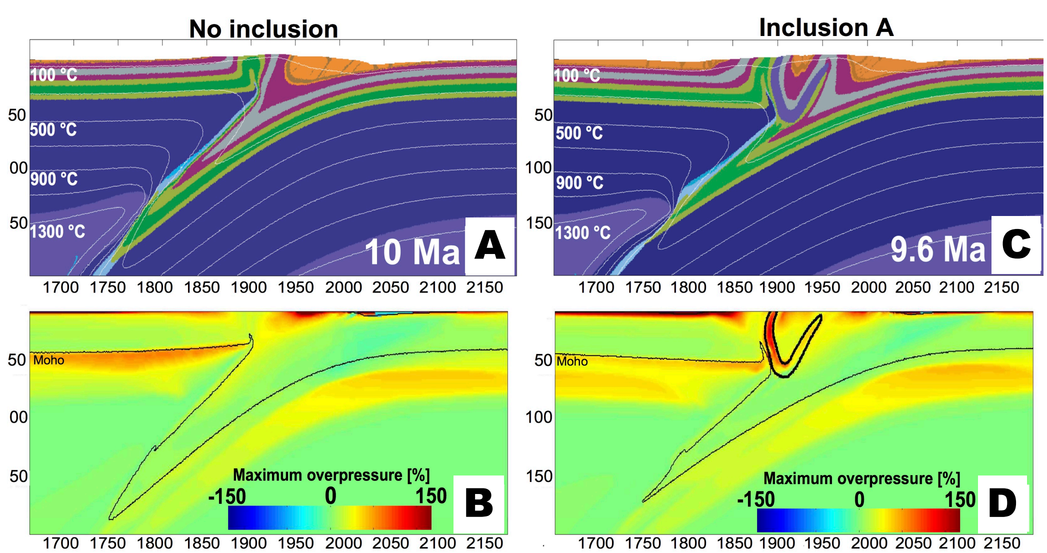


**Figure S5 | Simulations with homogeneous and heterogeneous crust:** A) Model evolution of a simulation with a homogeneous and weak crust, with an effective friction angle of 7° (as in Li et al. (2010)). B) The maximum non-lithostatic pressure that every marker experienced during the full model evolution after 10 Ma, normalized to the lithostatic pressure, which shows that the subduction channel is close to lithostatic in agreement with earlier results. C) Simulation in which a strong inclusion was inserted in the otherwise weak crust (inclusion A) and E) corresponding non-lithostatic pressure, which demonstrates that the exhumed heterogeneity has experienced significant non-lithostatic pressures.

## S4. Overview of systematic simulations

We have performed in total over 400 simulations, of which we compiled about 130 simulations in Table S2 as they are closely related to the model setup in the main paper. Simulations shown in figure 1 and 2 are highlighted in red, and simulations shown on Fig.S6 in green in the table.

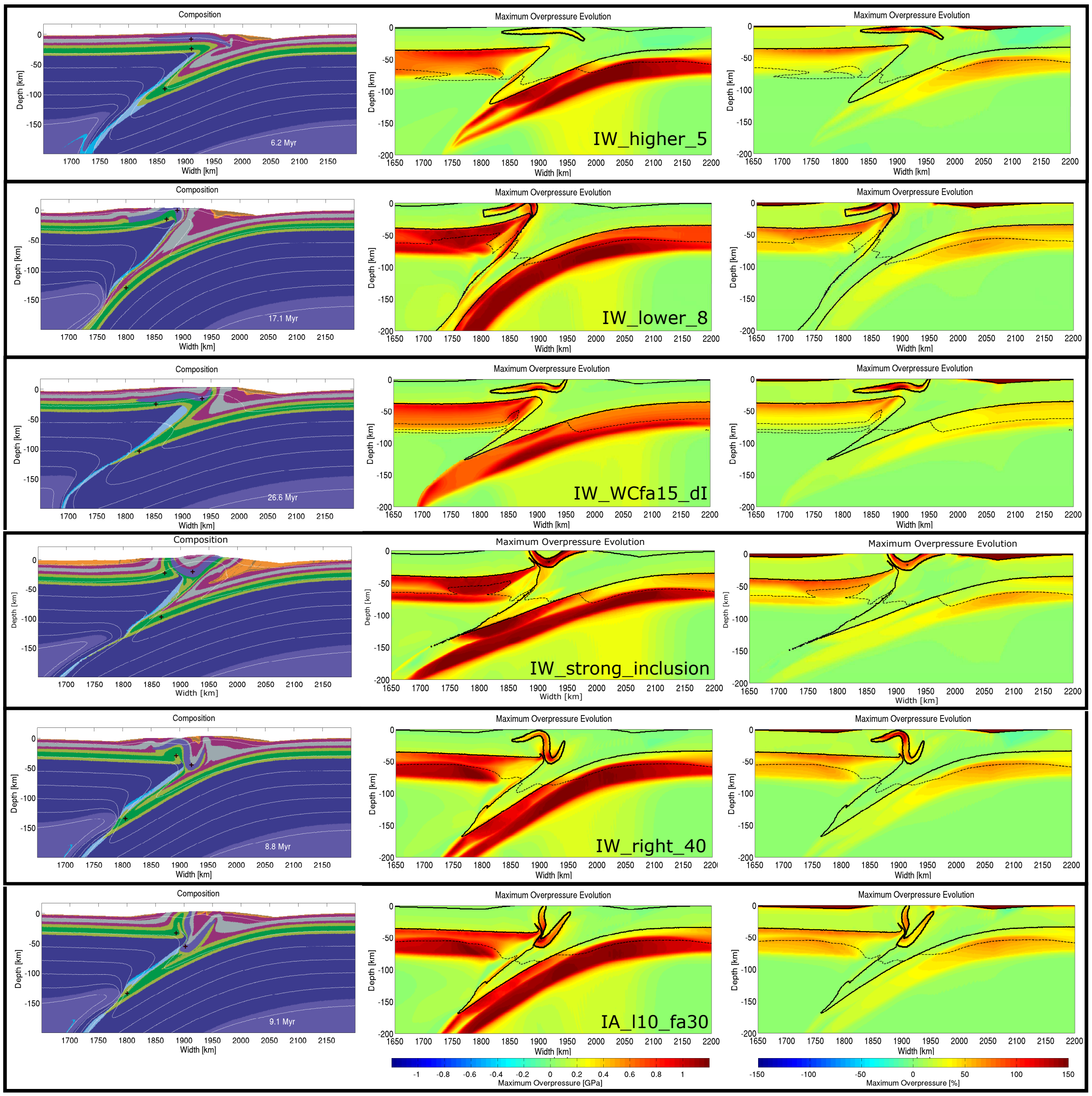


**Figure S6, Part 1 | Systematic simulations.** For each simulation, the geometry at the end of the simulation is shown (left), and the maximum overpressure particles experienced both in absolute and relative terms. Crosses indicate traced points that are used for the compilation of figure 2 (note that in figure only cases with a strong lower crust were included, but that all inclusion and weak subduction channel tracers are shown). Names in the middle column refer to Table S2.

283
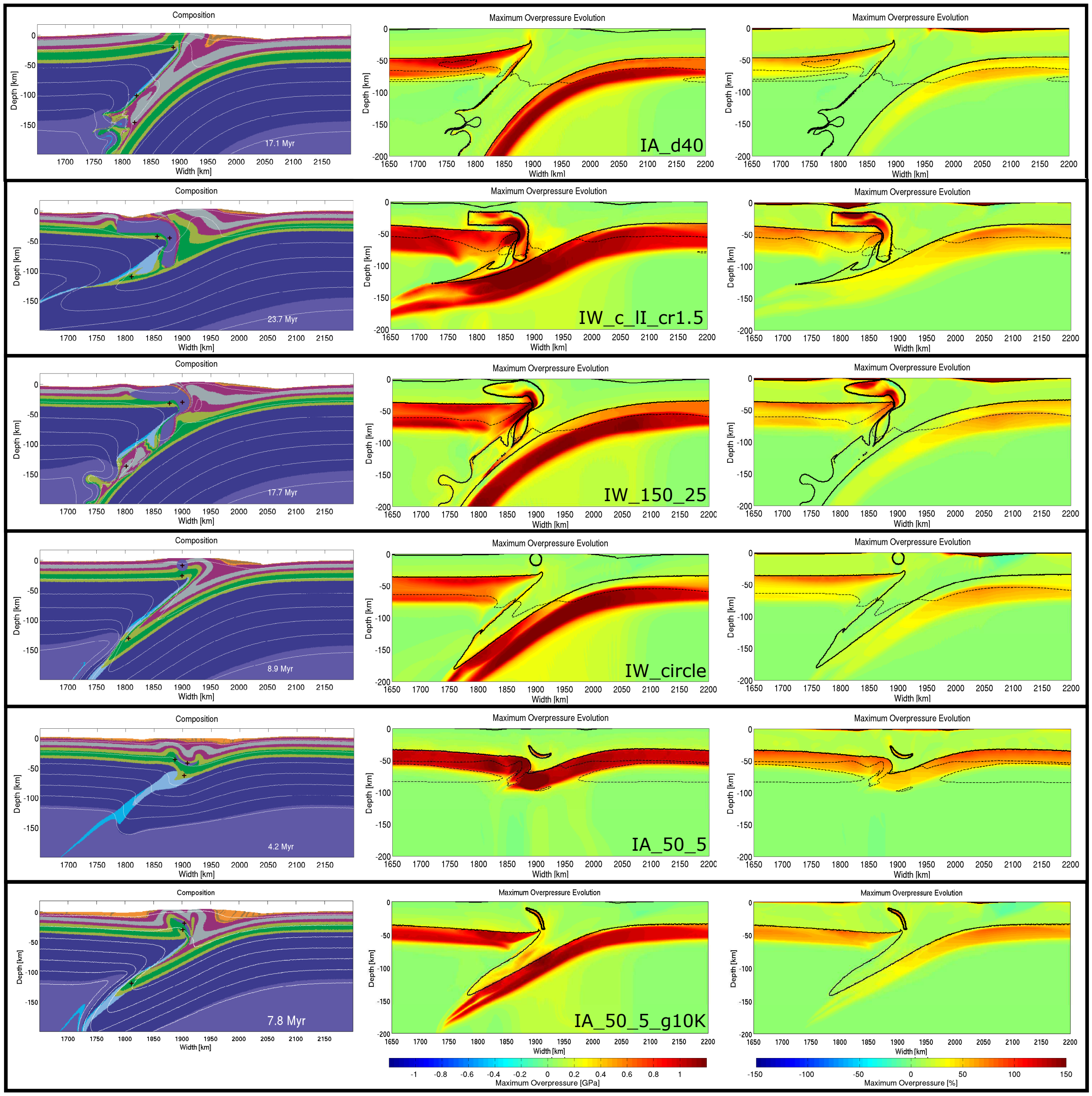


284 **Figure S6, Part 2 | Systematic simulations.**

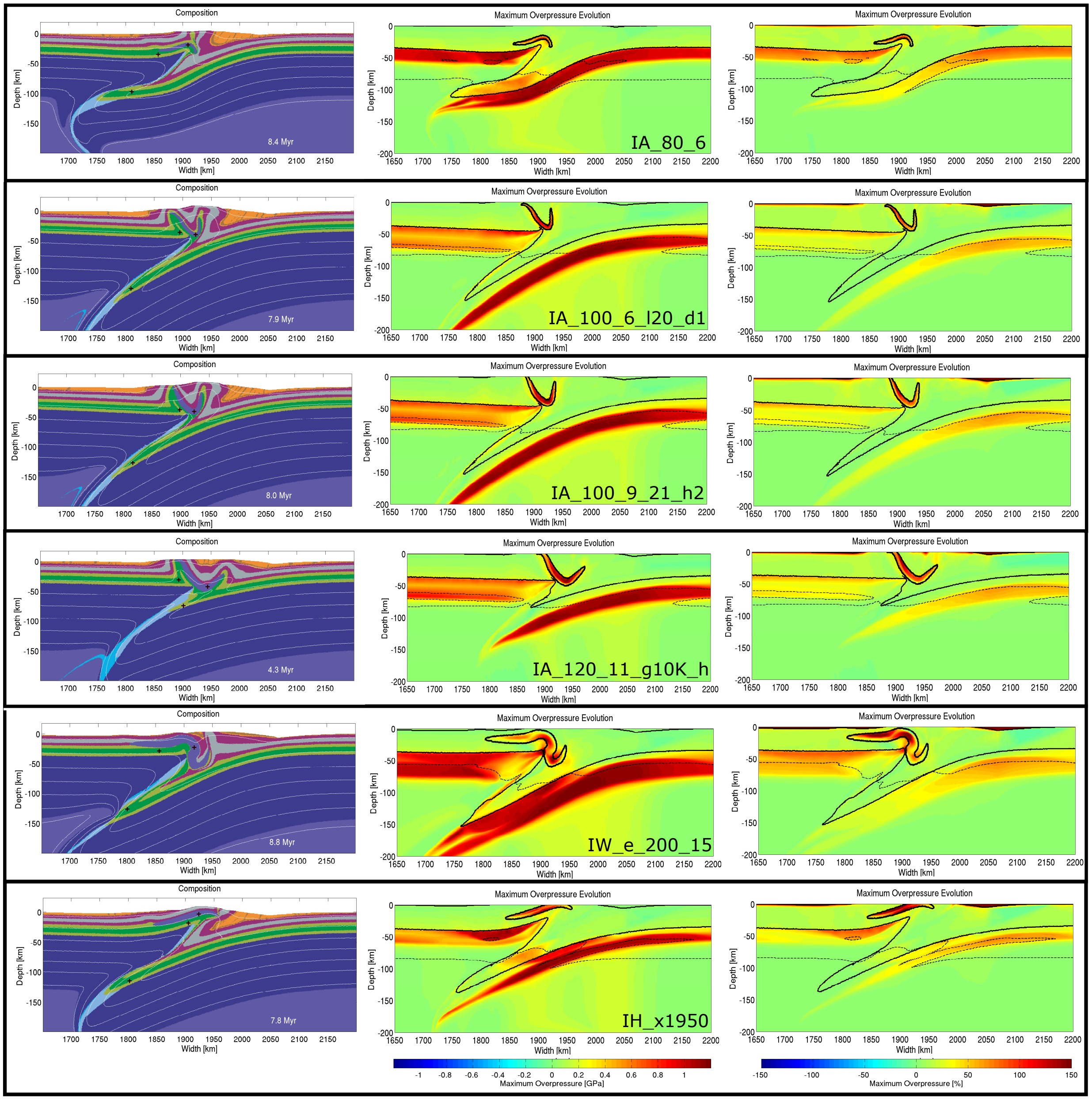


**Figure S6, Part 3 | Systematic simulations.**

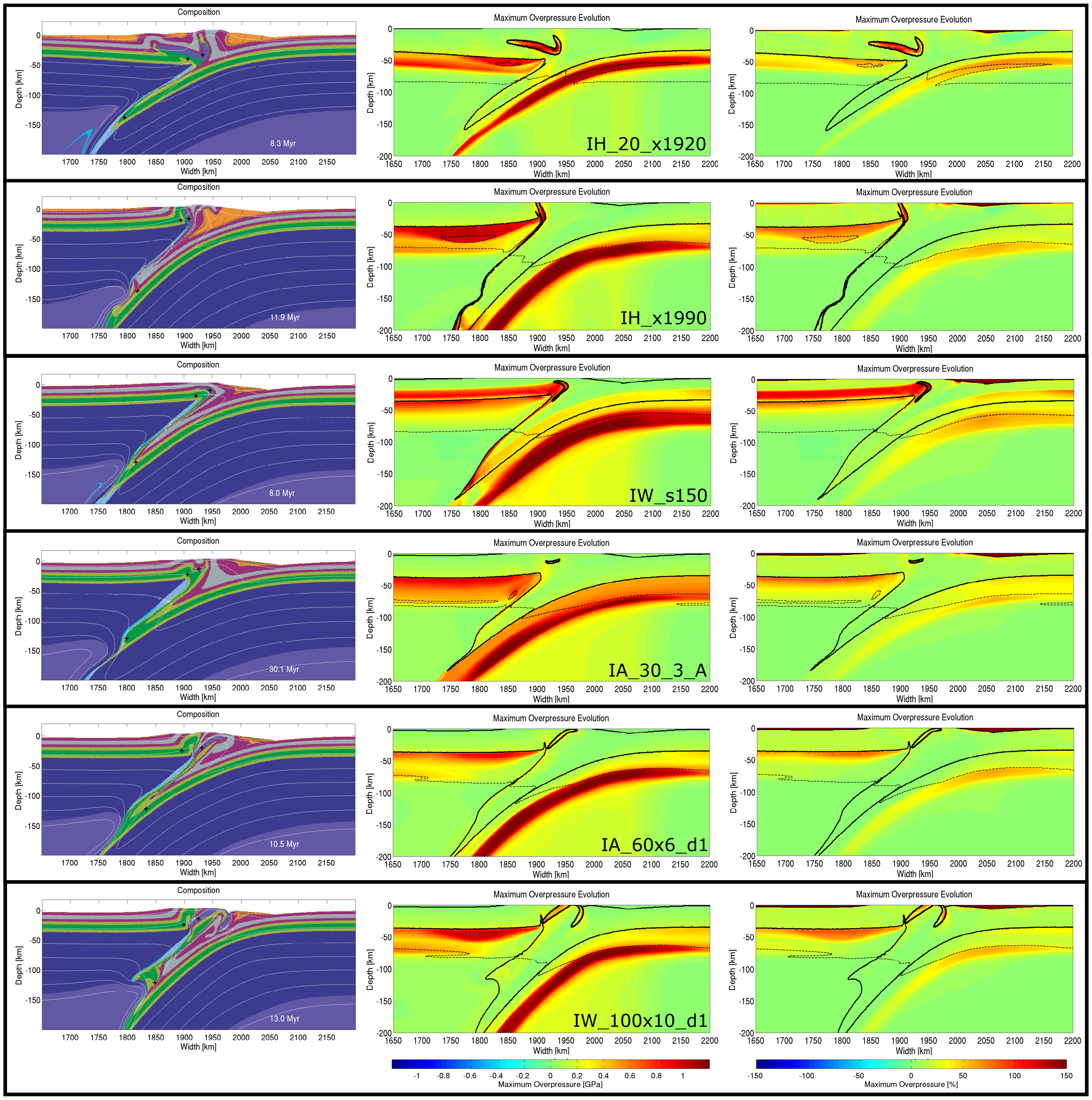


287

288 **Figure S6, Part 4 | Systematic simulations.**

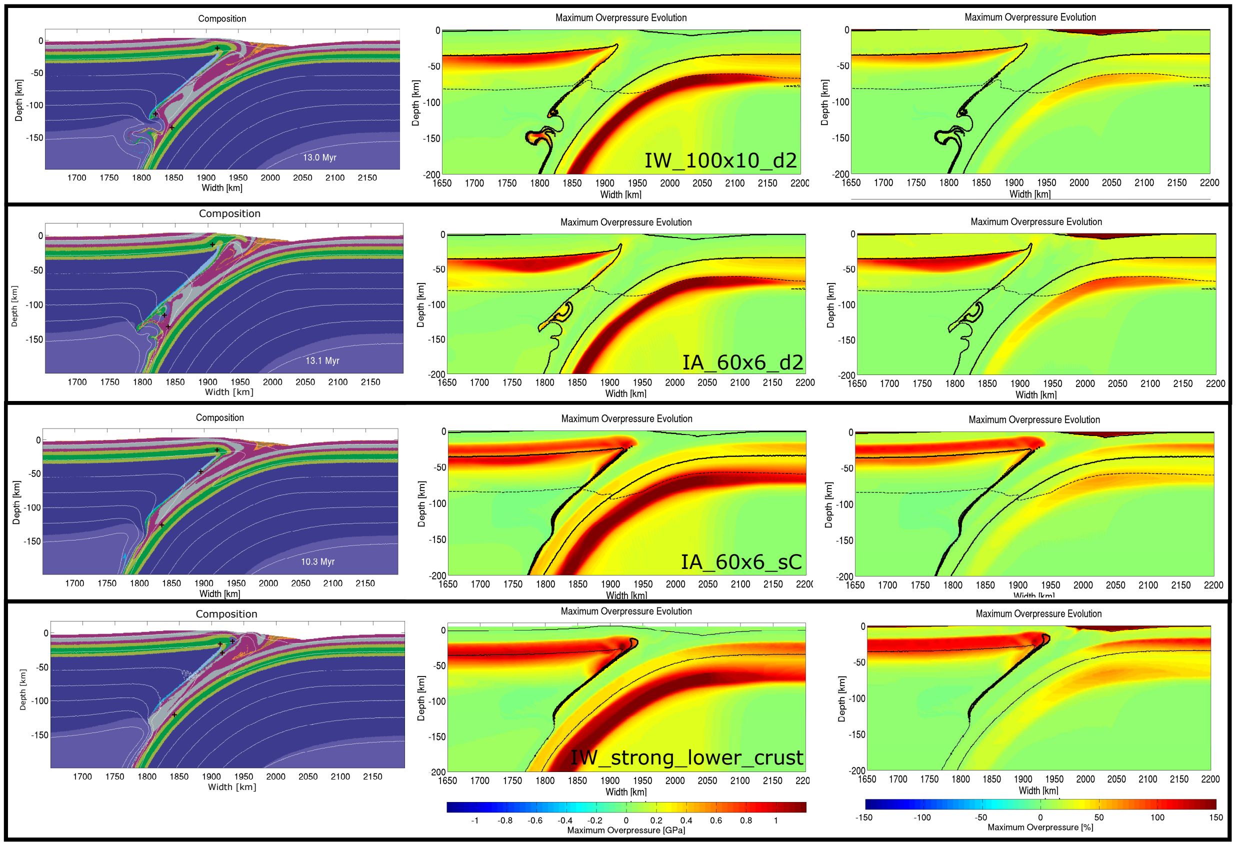


**Figure S6, Part 5 | Systematic simulations.**

The PT evolution of the tracers are shown on figure S7, whereas the temporal evolution of pressure and temperature is shown on figure S8.

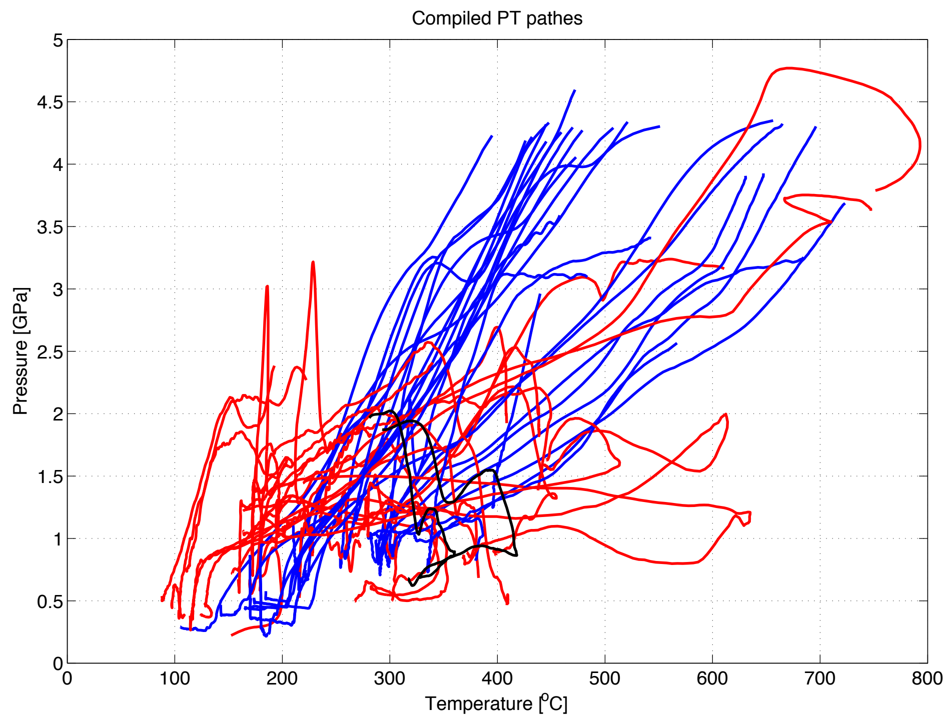


**Figure S7. PT-path of the systematic simulations shown in Fig 2.** Red lines refer to inclusions, blue lines to tracers within the subduction channel and black lines to tracers within the strong lower crust.

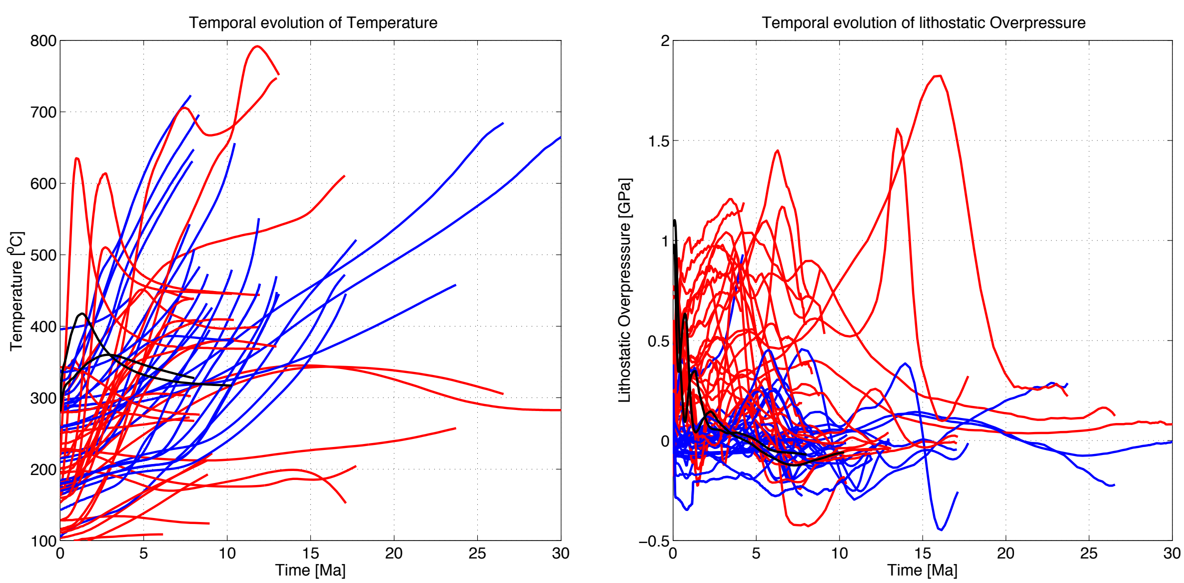


**Figure S8. Temporal evolution of temperature and pressure of tracers.** Strong fluctuations in the temperature curves are caused by a shear heating instability event, whereas a more gradual increase is caused by ordinary warming within a subduction channel. Fluctuations in pressure occur as a result of deformation of the inclusion and the evolution of the whole collision system.

## S5. Effect of elasticity

For consistency with the earlier results of Li et al. (2010) we performed most simulations with a viscoplastic rheology. Yet, real rocks have elastic effects as well and it is thus interesting to see whether the effects of elasticity significantly alter the results described here. We have therefore repeated the simulations shown on Fig. 1 with elasticity included (using an elastic shear module of $G$=$10^{11}$ Pa), starting from an initially stress-free state. Results show that the overall subduction geometry is largely the same, as is the shape of the heterogeneity (Fig. S9 and S10). The distribution of the overpressure areas is similar, even though peak pressures are slightly lower (in the strong inclusion case, we obtain a peak pressure of ~2.5 GPa, vs 2.6 GPa in the viscoplastic case). Some differences exist in the distribution of the deviatoric stresses, which we attribute to the fact that deformation was ongoing during the stress-buildup stage of our simulations.  In nature, it is unlikely that continental collision starts from an initially stress-free state, which would likely reduce the differences between the two endmember cases.

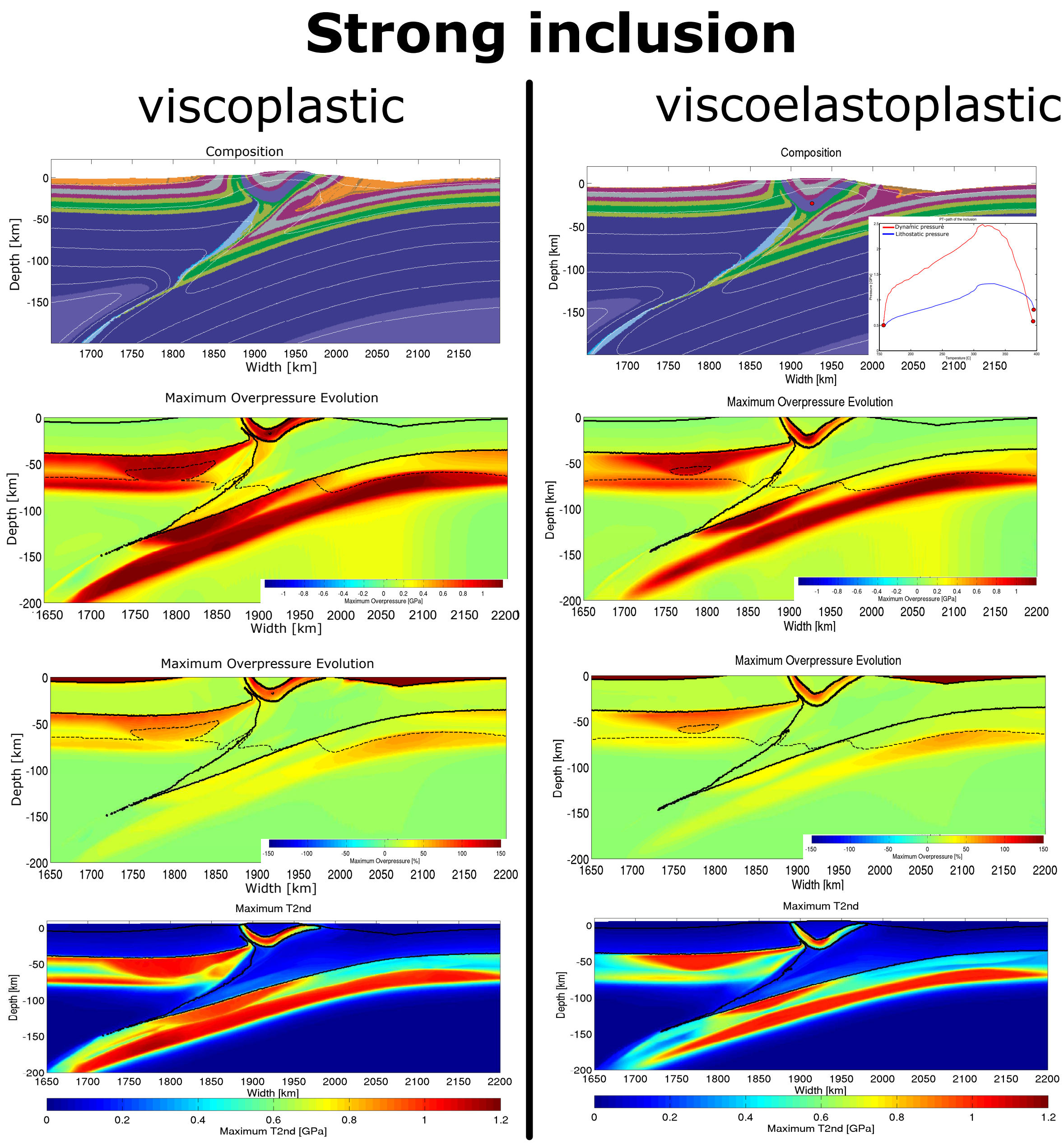


**Figure S9. Viscoplastic vs. viscoelastoplastic simulations for the case with a strong heterogeneity.** Left: the simulation shown on Figure 1a which has a viscoplastic rheology after 10.4 Ma. Right: the same simulation but with a viscoelastoplastic rheology after 10.0 Ma. Shown are the geometry, relative and absolute overpressure obtained throughout the simulation and the maximum of the second invariant of the deviatoric stress tensor achieved during the simulation. Inset shows a typical P-T path.

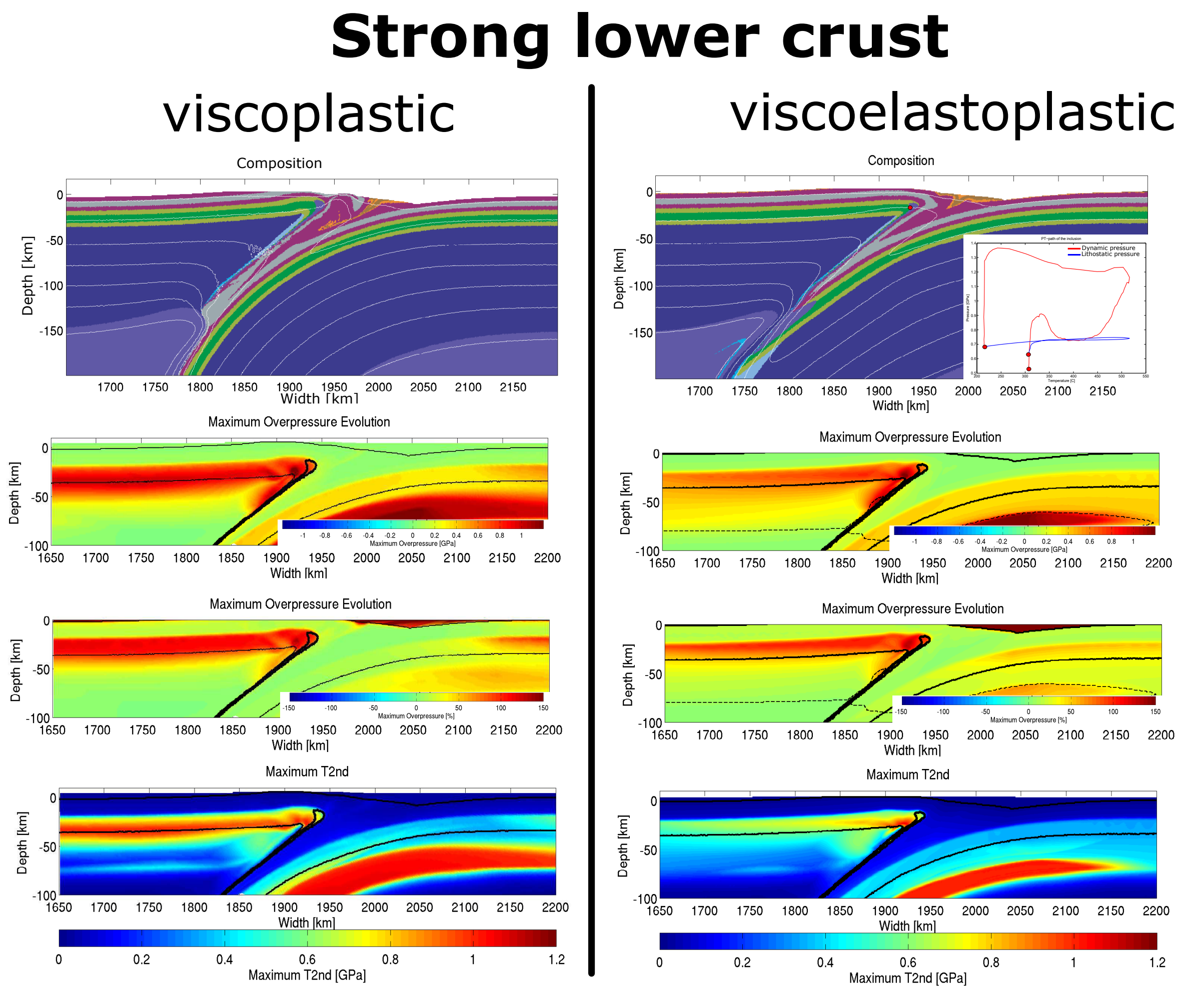


**Figure S10. Viscoplastic vs. viscoelastoplastic simulations for the case with a strong lower crust.** Left: the simulation shown on Figure 1b which has a viscoplastic rheology after 8.1 Ma. Right: the same simulation but with a viscoelastoplastic rheology after 8.0 Ma. Shown are the geometry, relative and absolute overpressure obtained throughout the simulation and the maximum of the second invariant of the deviatoric stress tensor achieved during the simulation. Inset shows a typical P-T path.

## References


Bittner, D., and Schmeling, H., 1995, Numerical modelling of melting processes and induced diapirism in the lower crust: Geophysical Journal International, v. 123, no. 1, p. 59–70.

Byerlee, J., 1978, Friction of rocks: Pure and Applied Geophysics, v. 116, p. 615–626.

Gerya, T., 2009, Introduction to Numerical Geodynamic Modelling: Cambridge.

Gerya, T.V., Stern, R.J., Baes, M., Sobolev, S.V., and Whattam, S.A., 2015, Plate tectonics on the Earth triggered by plume-induced subduction initiation: v. 527, no. 7577, p. 221–225, doi: 10.1038/nature15752.

Johnson, T.E., Brown, M., Kaus, B., and VanTongeren, J.A., 2014, Delamination and recycling of Archaean crust caused by gravitational instabilities: Nature Geoscience, v. 7, no. 1, p. 47–52, doi: 10.1038/NGEO2019.

Kaus, B., 2010, Factors that control the angle of shear bands in geodynamic numerical models of brittle deformation: Tectonophysics, v. 484, no. 1-4, p. 36–47, doi: 10.1016/j.tecto.2009.08.042.

Kirby, S.H., 1983, Rheology of the lithosphere: Reviews of Geophysics, v. 21, no. 6, p. 1458–1487, doi: 10.1029/RG021i006p01458.

Lockner, D.A., Morrow, C., Moore, D., and Hickman, S., 2011, Low strength of deep San Andreas fault gouge from SAFOD core: Nature, v. 472, no. 7341, p. 82–85, doi: 10.1038/nature09927.

Mackwell, S., and Zimmerman, M., 1998, High-temperature deformation of dry diabase with application to tectonics on Venus: Journal of Geophysical Research.

Ranalli, G., 1995, Rheology of the Earth: Chapman \& Hall, London ; New York :.

Ranalli, G., and Murphy, D.C., 1987, Rheological stratification of the lithosphere: Tectonophysics, v. 132, no. 4, p. 281–295.

Shelton, G., and Tullis, J., 1981, Shelton: Experimental flow laws for crustal rocks - Google Scholar: Eos Trans. AGU.

Thielmann, M., and Kaus, B., 2012, Shear heating induced lithospheric-scale localization Does it result in subduction?: Earth And Planetary Science Letters, v. 359-360, no. C, p. 1–13, doi: 10.1016/j.epsl.2012.10.002.

Thielmann, M., Kaus, B., and Popov, A.A., 2015, Lithospheric stresses in Rayleigh–Bénard convection: effects of a free surface and a viscoelastic Maxwell rheology: Geophysical Journal International, v. 203, no. 3, p. 2200–2219, doi: 10.1093/gji/ggv436.

Townend, J., and Zoback, M.D., 2000, How faulting keeps the crust strong: Geology, v. 28, no.

5, p. 399–402.

Turcotte, D.L., and Schubert, G., 2002, Geodynamics: Cambridge University Press.

Wilks, K.R., and Carter, N.L., 1990, Rheology of some continental lower crustal rocks: Tectonophysics, v. 182, no. 1-2, p. 57–77, doi: 10.1016/0040-1951(90)90342-6.

| Phase | $c_p$ [J/K] | k [W/(mK)] | Q [W/m$^3$] | $\rho_0$ [kg/m$^3$] | $\alpha$ [1/K] | $T_0$ [K] | C [Pa] | $\phi$ | flow law | A [MPa$^{-n}$s$^{-1}$] | n | E [kJ/mol] | V [m$^3$/mol] |
|---|---|---|---|---|---|---|---|---|---|---|---|---|---|
| Sediments | 1000 | 2.34 | 1.75e-6 | 2800 | 3e-5 | 293 | 1e6 | 8.6 | Wet Quartzite[1] | 3.2e-4 | 2.3 | 154 | 0 |
| Upper crust | 1000 | 2.34 | 1.75e-6 | 2800 | 3e-5 | 293 | 1e6 | 6.8 | Quartzite[1] | 6.7e-6 | 2.4 | 156 | 0 |
| Lower crust | 1000 | 1.97 | 2.5e-7 | 3000 | 3e-5 | 293 | 1e6 | 6.8* | Plagioclase (An 75)[2]* | 3.3e-4 | 3.2 | 238 | 0 |
| Lithosphere | 1000 | 1.99 | 2.2e-8 | 3300 | 3e-5 | 293 | 1e6 | 28.68 | Dry Olivine[3] | 2.5e4 | 3.5 | 532 | 17e-6 |
| Asthenosphere | 1000 | 1.99 | 2.2e-8 | 3300 | 3e-5 | 293 | 1e6 | 28.68 | Dry Olivine[3] | 2.5e4 | 3.5 | 532 | 17e-6 |
| Weak channel | 1000 | 2 | 0 | 3300 | 3e-5 | 293 | 1e6 | 3.44* | Wet Olivine[4] | 2e3 | 4 | 471 | 0 |
| Inclusion | 1000 | 2 | 0 | 3000* | 3e-5 | 293 | 1e6 | 36.9* | Mafic Granulite[5] | 1.4e4 | 4.2 | 445* | 0 |

TABLE S1: Table of used Parameters. Parameters with an asterisk were varied. Reading from left to right: Phase: phase name that is used in the simulations, $c_p$ [J/K]: heat capacity of the rock, k [W/(mK)]: conductivity of the rock, Q [W/m$^3$]: radioactive heat generation, $\rho_0$ [kg/m$^3$]: Density of the rock, $\alpha$ [1/K]: thermal expansion coefficient to compute the density of the rock, $T_0$ [K]: reference temperature used in the computation of the density, C [Pa]: Cohesion of the rock, $\phi$: friction angle of the rock, flow law: used flow law for this rock, A [MPa$^{-n}$s$^{-1}$]: prefactor used in the viscosity computation, E [kJ/mol]: Activation energy used in the viscosity computation, V [m$^3$/mol]: Activation volume used in the viscosity computation. Global parameters that were used: Adiabatic heating was used with $\alpha$ = 3e-5, Gravity is set to 10 [m/s$^2$], shear heating was used in all simulations except the reproduction of Li et al., 2010. [1]Ranalli and Murphy, 1987, [2]Shelton and Tullis, 1981, [3]Kirby, 1983, [4]Ranalli, 1995, [5]Wilks, 1990, Diabase rheology: Mackwell, 1998. Overall rheological parameters are assembled from Turcotte and Schubert, 2014, Li et al., 2010 and Bittner and Schmeling, 1995

| | $W_{inc}$ [km] | $H_{inc}$ [km] | MP(x) [km] | MP(z) [km] | Shape | $\phi$ | E [kJ /mol] | $\rho$ [kg /m$^3$] | Plate vel | OP mean | OP exhume | OP max | OP % | exhume [Ma] | Comments |
|---|---|---|---|---|---|---|---|---|---|---|---|---|---|---|---|
| IW_reference | 150 | 10 | 1920 | 15 | elliptical | 36.9 | 445 | 3000 | 3 | 0.36 | 0.8 | 0.9 | 60 | ~10 | complex bending of a large inclusion - L-shape |
| IW_higher_5 | -//- | -//- | -//- | 10 | -//- | -//- | -//- | -//- | -//- | 0.2 | 0.4 | 0.5 | 60 | ~5 | very fast exhumation - no subduction of incl. |
| IW_lower_5 | -//- | -//- | -//- | 20 | -//- | -//- | -//- | -//- | -//- | 0.4 | 0.7 | 1.1 | 60 | ~14 | break-off - upper part exhumed |
| IW_lower_8 | -//- | -//- | -//- | 23 | cuboid | 50° | -//- | -//- | -//- | 0.45 | 1 | 1.2 | 60 | ~17.5 | break-off - late exhumation upper part |
| IW_lower_10 | -//- | -//- | -//- | 25 | -//- | -//- | -//- | -//- | -//- | 0.44 | - | 1.5 | 60 | no | break-off - no exhumation |
| IW_lower_15 | -//- | -//- | -//- | 30 | -//- | -//- | -//- | -//- | -//- | 0.61 | - | 1.6 | 60 | no | break-off - no exhumation |
| IW_strong | -//- | -//- | -//- | -//- | -//- | -//- | 550 | -//- | -//- | 0.36 | 0.6 | 0.8 | 65 | ~10 | no subduction of incl. |
| IW_weak | -//- | -//- | -//- | -//- | -//- | -//- | 300 | -//- | -//- | 0.36 | 0.6 | 0.8 | 65 | ~10 | Inclusion flows in lower crust |
| IW_WCfa15 | -//- | -//- | -//- | -//- | -//- | -//- | -//- | -//- | -//- | 0.7 | 0.9 | 0.9 | 50 | ~6 | $\phi_{WC}$ = 15 - no subduction of incl. |
| IW_WCfa15_dI | -//- | -//- | -//- | 20 | -//- | -//- | -//- | -//- | -//- | 0.6 | 1 | 1 | 50 | ~9 | $\phi_{WC}$ = 15 - no subduction of incl. |
| IW_WCfa15_cr1 | -//- | -//- | -//- | 20 | -//- | -//- | -//- | -//- | 1 | 0.6 | 1 | 1 | 50 | ~25 | $\phi_{WC}$ = 15 - no subduction of incl. |
| IW_WCfa20 | -//- | -//- | -//- | -//- | -//- | -//- | -//- | -//- | -//- | 0.6 | 0.8 | 0.8 | 50 | ~6 | $\phi_{WC}$ = 20 - no subduction of incl. |
| IW_WCfa20_dI | -//- | -//- | -//- | 20 | -//- | -//- | -//- | -//- | -//- | 0.6 | 0.7 | 0.7 | 50 | ~14 | $\phi_{WC}$ = 20 - no subduction of incl. |
| IW_hfa_cub_lI | -//- | -//- | -//- | 22 | cuboid | 50 | -//- | -//- | 1.5 | 0.37 | - | 1.2 | 60 | no | locking of subduction zone |
| IW_hfa_sur45 | -//- | -//- | -//- | 27 | cuboid | 50 | -//- | -//- | 1.5 | 0.7 | 0.9 | 1.1 | 65 | ~5 | $\phi_{LC}$ = 45 - break-off |
| IW_hfa_sur45_2 | -//- | -//- | -//- | 18 | cuboid | 50 | -//- | -//- | 1.5 | 0.6 | 0.7 | 0.9 | 60 | ~3 | $\phi_{LC}$ = 45 - break-off - strong topo |
| IW_cuboid | -//- | -//- | -//- | -//- | cuboid | -//- | -//- | -//- | -//- | 0.4 | 0.7 | 1.1 | 60 | ~9.6 | break-off |
| IW_high_fa | -//- | -//- | -//- | -//- | -//- | 50 | -//- | -//- | -//- | 0.37 | 0.6 | 1 | 60 | ~12 | complex bending of a large inclusion - L-shape |
| IW_low_fa | -//- | -//- | -//- | -//- | -//- | 25 | -//- | -//- | -//- | 0.3 | 0.4 | 0.5 | 60 | ~12 | complex bending of a large inclusion - L-shape |
| IW_e_150_10 | -//- | -//- | 2065 | -//- | -//- | -//- | -//- | -//- | -//- | 0.36 | - | 0.8 | 30 | no | fast subduction of incl. - almost no bending |
| IW_sur45 | -//- | -//- | -//- | -//- | -//- | -//- | -//- | -//- | -//- | 0.8 | 0.9 | 1 | 70 | ~4.5 | complex bending of a large inclusion - L-shape - strong topo |
| Inclusion A | -//- | -//- | 2020 | -//- | -//- | -//- | -//- | -//- | -//- | 0.3 | 0.5 | 1.2 | 60 | ~2.5 | complex bending of a large inclusion - V-shape |
| IW_150_10_l | -//- | -//- | -//- | -//- | -//- | -//- | -//- | 2800 | -//- | 0.37 | 0.9 | 0.95 | 65 | ~8 | complex bending of a large inclusion - L-shape |
| IW_150_10_h | -//- | -//- | -//- | -//- | -//- | -//- | -//- | 3200 | -//- | 0.35 | 0.9 | 0.95 | 65 | ~15 | complex bending of a large inclusion - L-shape |
| IA_cr1.5 | -//- | -//- | 2030 | -//- | -//- | -//- | -//- | -//- | 1.5 | 0.3 | 0.3 | 1.5 | 20 | ~36 | complex bending of a large inclusion - V-shape |
| IW_right_40 | -//- | -//- | 1960 | -//- | -//- | -//- | -//- | -//- | -//- | 0.3 | 0.8 | 0.97 | 60 | ~8 | double bending of inclusion - huge influence of incl. on subduction |

| | $W_{inc}$ [km] | $H_{inc}$ [km] | MP(x) [km] | MP(z) [km] | Shape | $\phi$ | E [kJ /mol] | $\rho$ [kg $/m^3$] | Plate vel | OP mean | OP exhume | OP max | OP % | exhume [Ma] | Comments |
|---|---|---|---|---|---|---|---|---|---|---|---|---|---|---|---|
| IW_reference | 150 | 10 | 1920 | 15 | elliptical | 36.9 | 445 | 3000 | 3 | 0.36 | 0.8 | 0.9 | 60 | ∼10 | complex bending of a large inclusion - L-shape |
| IW_left_20_2 | -//- | -//- | 1900 | -//- | -//- | -//- | -//- | -//- | -//- | 0.25 | 0.3 | 0.5 | 50 | ∼12.5 | no bending - no subduction of incl. |
| IW_cr1.5 | -//- | -//- | -//- | -//- | -//- | -//- | -//- | -//- | 1.5 | 0.33 | 0.9 | 0.9 | 65 | ∼10 | complex bending of a large inclusion - L-shape |
| IW_cr5 | -//- | -//- | -//- | -//- | -//- | -//- | -//- | -//- | 5 | 0.33 | 0.6 | 0.6 | 60 | ∼25 | complex bending of a large inclusion - L-shape |
| IA_d30 | -//- | -//- | 2030 | 30 | -//- | -//- | -//- | -//- | -//- | 0.6 | - | 1.4 | 30 | no | complex bending of a large inclusion - V-shape - no exhumation |
| IA_d40 | -//- | -//- | 2030 | 40 | -//- | -//- | -//- | -//- | -//- | 0.4 | - | 0.6 | 25 | no | fast subduction of incl. - almost no bending |
| IA_l10_fa30 | -//- | -//- | 2020 | -//- | -//- | 30 | -//- | -//- | -//- | 0.4 | 0.3 | 1 | 40 | ∼9 | complex bending of a large inclusion - V-shape |
| IA_l10_12K | -//- | -//- | 2020 | -//- | -//- | -//- | -//- | -//- | -//- | 0.4 | - | 1.1 | 35 | no | 12K geotherm - V-shape - no exhumation |
| IA_l15 | -//- | -//- | 2015 | -//- | -//- | -//- | -//- | -//- | -//- | 0.4 | 0.3 | 1.3 | 30 | ∼9 | complex bending of a large inclusion - V-shape |
| IA_l20 | -//- | -//- | 2010 | -//- | -//- | -//- | -//- | -//- | -//- | 0.4 | 1.2 | 1.2 | 35 | ∼2.7 | complex bending of a large inclusion - V-shape - |
| IA_l30 | -//- | -//- | 2000 | -//- | -//- | -//- | -//- | -//- | -//- | 0.4 | 1.2 | 1.2 | 40 | ∼2.7 | complex bending of a large inclusion - V-shape |
| IW_150_15 | -//- | 15 | -//- | -//- | -//- | -//- | -//- | -//- | -//- | 0.32 | 0.4 | 0.9 | 60 | ∼10 | complex bending of a large inclusion - L-shape |
| IW_150_20 | -//- | 20 | -//- | -//- | -//- | -//- | -//- | -//- | -//- | 0.29 | 0.4 | 1 | 60 | no | huge influence of incl. on subduction |
| IW_left_5 | -//- | 20 | 1915 | -//- | -//- | -//- | -//- | -//- | -//- | 0.3 | 0.5 | 0.9 | 60 | ∼11.5 | complex bending of a large inclusion - L-shape |
| IW_left_10 | -//- | 20 | 1910 | -//- | -//- | -//- | -//- | -//- | -//- | 0.22 | 0.4 | 0.8 | 60 | ∼11.5 | only small piece subducts |
| IW_left_20 | -//- | 20 | 1900 | -//- | -//- | -//- | -//- | -//- | -//- | 0.22 | 0.4 | 0.65 | 55 | ∼11.5 | no bending - no subduction of incl. |
| IW_right_5 | -//- | 20 | 1925 | -//- | -//- | -//- | -//- | -//- | -//- | 0.3 | 0.5 | 1.1 | 60 | ∼17.5 | complex bending of a large inclusion - L-shape |
| IW_right_10 | -//- | 20 | 1930 | -//- | -//- | -//- | -//- | -//- | -//- | 0.33 | - | 1 | 60 | no | complex bending of a large inclusion - L-shape |
| IW_20_cr1.5 | -//- | 20 | -//- | -//- | -//- | -//- | -//- | -//- | 1.5 | 0.28 | 0.4 | 1.2 | 65 | ∼6.5 | complex bending of a large inclusion - L-shape |
| IW_20_cr5 | -//- | 20 | -//- | -//- | -//- | -//- | -//- | -//- | 5 | 0.29 | - | 0.9 | 65 | no | huge influence of incl. on subduction - locking of subduction zone |
| IW_c_lI_cr1.5 | -//- | 20 | -//- | 17 | cuboid | 50 | -//- | -//- | 1.5 | 0.5 | - | 2 | 45 | no | locking of subduction zone |
| IW_c_dI_cr1.5 | -//- | 20 | -//- | 18 | cuboid | 50 | -//- | -//- | 1.5 | 0.5 | - | 1.6 | 40 | no | locking of subduction zone |

| | $W_{inc}$ [km] | $H_{inc}$ [km] | MP(x) [km] | MP(z) [km] | Shape | $\phi$ | E [kJ /mol] | $\rho$ [kg /m$^3$] | Plate vel | OP mean | OP exhume | OP max | OP % | exhume [Ma] | Comments |
|---|---|---|---|---|---|---|---|---|---|---|---|---|---|---|---|
| IW_reference | 150 | 10 | 1920 | 15 | elliptical | 36.9 | 445 | 3000 | 3 | 0.36 | 0.8 | 0.9 | 60 | ∼10 | complex bending of a large inclusion - L-shape |
| IW_150_25 | -//- | 25 | -//- | -//- | -//- | -//- | -//- | -//- | -//- | 0.3 | 0.4 | 1.1 | 60 | ∼13 | huge influence of inclusion on subduction - less bending of incl. |
| IW_c_lI2_cr1.5 | -//- | 25 | -//- | 17 | cuboid | 50 | -//- | -//- | 1.5 | 0.5 | - | 1.3 | 40 | no | locking of subduction zone |
| IW_c_dI2_cr1.5 | -//- | 25 | -//- | 18 | cuboid | 50 | -//- | -//- | 1.5 | 0.5 | - | 1.3 | 40 | no | locking of subduction zone |
| IA_10_2 | 10 | 2 | 1980 | -//- | -//- | -//- | -//- | -//- | -//- | 0.05 | 0.1 | 0.1 | 0 | 5 | no influence of incl. |
| IA_20_2 | 20 | 2 | 1990 | 20 | -//- | -//- | -//- | -//- | -//- | 0.15 | - | 0.3 | 0 | no | no influence of incl. - subduction of incl. |
| IA_20_2_g10K | 20 | 2 | 1990 | 40 | -//- | -//- | -//- | 2800 | 1.5 | 0.05 | - | 0.1 | 0 | no | 10K geotherm - no influence of incl. - no subduction process |
| IW_20_5_r20 | 20 | 5 | 1940 | 35 | -//- | -//- | -//- | -//- | -//- | 0.6 | - | 0.8 | 40 | no | inclusion stays at the subduction neck |
| IW_20_5_r30 | 20 | 5 | 1950 | 35 | -//- | -//- | -//- | -//- | -//- | 0.6 | - | 0.8 | 40 | no | inclusion subducts completely |
| IW_20_5_r40 | 20 | 5 | 1960 | 35 | -//- | -//- | -//- | -//- | -//- | 0.6 | - | 0.8 | 40 | no | inclusion subducts completely |
| IW_20_10 | 20 | 10 | -//- | -//- | -//- | -//- | -//- | -//- | -//- | 0.17 | 0.1 | 0.2 | 50 | ∼7 | fast exhumation - no bending |
| IW_c_sI_cr1.5 | 20 | 10 | -//- | 17 | cuboid | 50 | -//- | -//- | 1.5 | 0.1 | 0.1 | 0.2 | 40 | ∼17.5 | large aspect ratio - low OP |
| IW_c_sI_cr1.5 | 20 | 10 | -//- | 17 | cuboid | 50 | -//- | -//- | 1.5 | 0.1 | 0.1 | 0.2 | 40 | ∼17.5 | large aspect ratio - low OP |
| IW_circle | 20 | 20 | -//- | -//- | -//- | -//- | -//- | -//- | -//- | 0.17 | 0.2 | 0.2 | 50 | ∼4.5 | fast exhumation - no bending |
| IW_square | 20 | 20 | -//- | -//- | cuboid | -//- | -//- | -//- | -//- | 0.15 | 0.2 | 0.2 | 50 | ∼4.5 | fast exhumation - no bending |
| IA_30_3 | 30 | 3 | 1980 | 20 | -//- | -//- | -//- | -//- | 1 | 0.4 | - | 0.7 | 20 | no | $\phi_{WC}$ = 10 - complex bending o. small I. |
| IA_30_3_f15 | 30 | 3 | 1980 | 20 | -//- | -//- | -//- | -//- | 1 | 0.4 | - | 0.7 | 20 | no | $\phi_{WC}$ = 15 - complex bending o. small I. |
| IA_30_3_f20 | 30 | 3 | 1980 | 20 | -//- | -//- | -//- | -//- | 1 | 0.4 | - | 0.7 | 20 | no | $\phi_{WC}$ = 20 - complex bending o. small I. |
| IA_30_3_d | 30 | 3 | 1980 | 30 | -//- | -//- | -//- | -//- | 1 | 0.3 | - | 0.6 | 20 | no | $\phi_{WC}$ = 15 - complex bending o. small I. |
| IA_30_3_A | 30 | 3 | 1970 | 20 | -//- | -//- | -//- | -//- | 1 | 0.3 | - | 0.5 | 30 | no | $\phi_{WC}$ = 15 - complex bending o. small I. |
| IA_40_4 | 40 | 4 | 1980 | 20 | -//- | -//- | -//- | -//- | 1 | 0.3 | - | 0.6 | 30 | no | $\phi_{WC}$ = 40 - complex bending o. small I. |
| IA_50_5 | 50 | 5 | -//- | -//- | -//- | -//- | -//- | -//- | -//- | 0.2 | - | 0.4 | 50 | no | 12K geotherm - Diabase rheology lower crust |
| IA_50_5_g11K | 50 | 5 | 1961 | 22 | -//- | -//- | -//- | -//- | -//- | 0.1 | 0.4 | 0.4 | 30 | ∼14 | 11K geotherm - Diabase rheology lower crust |
| IA_s150 | 50 | 5 | 1961 | 18 | -//- | -//- | -//- | -//- | -//- | 0.8 | 0.8 | 0.8 | 100 | ∼10 | $\phi_{LC}$ = 30 - L-shape |
| IA_50_5_g10K | 50 | 5 | 1961 | 18 | -//- | -//- | -//- | -//- | -//- | 0.7 | - | 0.9 | 30 | no | 10K geotherm - Diabase rheology lower crust - $\phi_{LC}$ = 30 - L-shape - locking of subduction zone |

| | $W_{inc}$ [km] | $H_{inc}$ [km] | MP(x) [km] | MP(z) [km] | Shape | $\phi$ | E [kJ /mol] | $\rho$ [kg /m$^3$] | $Pl_{vel}$ [cm/a] | OP mean | OP exhume | OP max | OP % | exhume [Ma] | Comments |
|---|---|---|---|---|---|---|---|---|---|---|---|---|---|---|---|
| IW_reference | 150 | 10 | 1920 | 15 | elliptical | 36.9 | 445 | 3000 | 3 | 0.36 | 0.8 | 0.9 | 60 | ∼10 | complex bending of a large inclusion - L-shape |
| IA_60_6_d1 | 60 | 6 | 2030 | 13 | -//- | -//- | -//- | -//- | -//- | 0.25 | 0.3 | 0.3 | 25 | ∼13 | small bending of incl. - no subduction of incl. |
| IA_60_6_d2 | 60 | 6 | 2050 | 13 | -//- | -//- | -//- | -//- | -//- | 0.4 | - | 0.6 | 10 | no | fast subduction of incl. - bending of incl. in the mantle |
| IA_60_6_sC | 60 | 6 | 1980 | 22 | -//- | -//- | -//- | -//- | -//- | 0.7 | - | 1 | 50 | no | $\phi_{LC} = 30$ - fast subduction of incl. |
| IA_60_8 | 60 | 8 | 1950 | 18 | -//- | -//- | -//- | -//- | -//- | 0.05 | 0.1 | 0.1 | 25 | ∼8 | 12K geotherm - Diabase rheology lower crust - no subduction of incl. |
| IA_80_6 | 80 | 6 | 1920 | 25 | -//- | -//- | -//- | -//- | -//- | 0.4 | - | 0.6 | 50 | no | 12K geotherm - Diabase rheology lower crust |
| IA_100_6 | 100 | 6 | -//- | 25 | -//- | -//- | -//- | -//- | -//- | 0.3 | - | 0.9 | 0 | no | 12K geotherm - Diabase rheology lower crust - L-shape |
| IA_100_6_l20 | 100 | 6 | 1970 | 22 | -//- | 40 | -//- | -//- | -//- | 0.6 | 0.5 | 1 | 35 | ∼8 | Diabase rheology lower crust - V-shape |
| IA_100_6_l10 | 100 | 6 | 1980 | 22 | -//- | 40 | -//- | -//- | -//- | 0.6 | 0.5 | 1 | 35 | ∼11 | Diabase rheology lower crust - V-shape |
| IA_100_6_l20_g9K | 100 | 6 | 1970 | 22 | -//- | 40 | -//- | -//- | -//- | 0.6 | 0.5 | 1 | 35 | ∼12 | 9K geotherm - Diabase rheology lower crust - V-shape |
| IA_100_6_l10_g9k | 100 | 6 | 1980 | 22 | -//- | 40 | -//- | -//- | -//- | 0.6 | 0.5 | 1 | 35 | ∼13 | 9K geotherm - Diabase rheology lower crust - V-shape |
| IA_100_6_l20_d1 | 100 | 6 | 1970 | 23 | -//- | 40 | -//- | -//- | -//- | 0.6 | 0.5 | 1 | 35 | ∼12 | Diabase rheology lower crust - V-shape |
| IA_100_6_l10_d1 | 100 | 6 | 1980 | 23 | -//- | 40 | -//- | -//- | -//- | 0.6 | 0.5 | 1 | 35 | ∼13 | Diabase rheology lower crust - V-shape |
| IA_100_6_l20_d2 | 100 | 6 | 1970 | 23 | -//- | 40 | -//- | -//- | -//- | 0.6 | 0.5 | 1 | 35 | ∼13 | 9K geotherm - Diabase rheology lower crust - V-shape |
| IA_100_6_l10_d2 | 100 | 6 | 1980 | 22 | -//- | 40 | -//- | -//- | -//- | 0.6 | 0.5 | 1 | 35 | ∼14 | 9K geotherm - Diabase rheology lower crust - V-shape |
| IA_100_8 | 100 | 8 | -//- | 25 | -//- | -//- | -//- | -//- | -//- | 0.4 | - | 0.9 | 0 | no | 12K geotherm - Diabase rheology lower crust - L-shape |
| IA_100_9_h | 100 | 9 | 1990 | 22 | -//- | 45 | -//- | -//- | -//- | 0.5 | - | >1.2 | 30 | no | Diabase rheology lower crust - 9K geotherm - V-shape - incl. close to surface |
| IA_100_9_h2 | 100 | 9 | 1990 | 22 | -//- | 50 | -//- | -//- | -//- | 0.6 | - | >1.2 | 30 | no | Diabase rheology lower crust - 9K geotherm - V-shape - incl. close to surface |
| IA_100_9_r10_h | 100 | 9 | 2000 | 22 | -//- | 45 | -//- | -//- | -//- | 0.6 | - | >1.2 | 30 | no | Diabase rheology lower crust - 9K geotherm - V-shape - incl. completely subducts |
| IA_100_9_r10_h2 | 100 | 9 | 2000 | 22 | -//- | 50 | -//- | -//- | -//- | 0.6 | - | >1.2 | 30 | ∼11 | Diabase rheology lower crust - 9K geotherm - V-shape - incl. completely subducts |

| | $W_{inc}$ [km] | $H_{inc}$ [km] | MP(x) [km] | MP(z) [km] | Shape | $\phi$ | E [kJ /mol] | $\rho$ [kg /m$^3$] | $Pl_{vel}$ [cm/a] | OP mean | OP exhume | OP max | OP % | exhume [Ma] | Comments |
|---|---|---|---|---|---|---|---|---|---|---|---|---|---|---|---|
| IW_reference | 150 | 10 | 1920 | 15 | elliptical | 36.9 | 445 | 3000 | 3 | 0.36 | 0.8 | 0.9 | 60 | ~10 | complex bending of a large inclusion - L-shape |
| IA_100_9_h3 | 100 | 9 | 1990 | 22 | -//- | 45 | -//- | -//- | -//- | 0.5 | 0.3 | >1.2 | 35 | ~12 | Diabase rheology lower crust - V-shape |
| IA_100_9_r10_h3 | 100 | 9 | 2000 | 22 | -//- | 45 | -//- | -//- | -//- | 0.7 | - | >1.2 | 35 | no | Diabase rheology lower crust - V-shape - incl. completely subducts |
| IA_100_9_r10_h4 | 100 | 9 | 2000 | 22 | -//- | 50 | -//- | -//- | -//- | 0.7 | - | >1.2 | 35 | no | Diabase rheology lower crust - V-shape - incl. completely subducts |
| IA_100_9_h4 | 100 | 9 | 1990 | 22 | -//- | 50 | -//- | -//- | -//- | 0.6 | 0.4 | >1.2 | 35 | ~12 | Diabase rheology lower crust - V-shape |
| IA_100_9_21_h | 100 | 9 | 1980 | 21 | -//- | 50 | -//- | -//- | -//- | 0.6 | 0.4 | >1.2 | 35 | ~8 | Diabase rheology lower crust - 8K geotherm - V-shape |
| IA_100_9_21_h2 | 100 | 9 | 1980 | 21 | -//- | 50 | -//- | -//- | -//- | 0.5 | 0.4 | >1.2 | 35 | ~5 | Diabase rheology lower crust - 9K geotherm - V-shape |
| IH_x1990 | 100 | 9 | 1990 | 22 | -//- | 45 | -//- | -//- | -//- | 0.6 | 0.9 | 0.9 | 60 | ~12 | Diabase rheology lower crust - 9K geotherm - V-shape |
| IW_hfa_cub | 100 | -//- | -//- | 22 | cuboid | 50 | -//- | -//- | 1.5 | 0.3 | 0.8 | 1 | 50 | ~23 | break-off - upper part exhumed |
| IW_100_10 | 100 | -//- | -//- | -//- | -//- | -//- | -//- | -//- | -//- | 0.24 | 0.4 | 0.5 | 60 | ~10 | very fast exhumation - no subduction of incl. |
| IW_100_10_d1 | 100 | -//- | 2030 | 13 | -//- | -//- | -//- | -//- | -//- | 0.3 | 0.5 | 0.5 | 35 | ~10 | no subduction of incl. |
| IW_100_10_d2 | 100 | -//- | 2030 | 21 | -//- | -//- | -//- | -//- | -//- | 0.3 | - | 0.6 | 10 | no | fast subduction of incl. |
| IW_100_15 | 100 | 15 | -//- | -//- | -//- | -//- | -//- | -//- | -//- | 0.22 | 0.4 | 0.5 | 50 | ~10 | very fast exhumation - no subduction of incl. |
| IW_100_20 | 100 | 20 | -//- | -//- | -//- | -//- | -//- | -//- | -//- | 0.21 | 0.4 | 0.4 | 30 | ~10 | very fast exhumation - no bending |
| IA_120_8 | 120 | 8 | 1970 | -//- | -//- | -//- | -//- | -//- | -//- | 0.6 | 0.6 | 0.6 | 50 | ~10 | 11K geotherm - Diabase rheology lower crust - no subduction of incl. |
| IA_120_8_g11K | 120 | 8 | 1970 | 20 | -//- | -//- | -//- | -//- | -//- | 0.35 | 0.1 | 0.8 | 30 | ~10 | 11K geotherm - Diabase rheology lower crust - no subduction of incl. - upwards bending |
| IA_120_10_g11K | 120 | 10 | -//- | 20 | -//- | -//- | -//- | -//- | -//- | 0.5 | 0.5 | 0.5 | 40 | ~10 | 11K geotherm - Diabase rheology lower crust - L-shape |
| IA_120_10_g11K | 120 | 10 | -//- | 25 | -//- | -//- | -//- | -//- | -//- | 0.5 | - | 0.5 | 40 | no | 11K geotherm - Diabase rheology lower crust - L-shape - locking of subduction zone |
| IA_120_10_g13K | 120 | 10 | -//- | 18 | -//- | -//- | -//- | -//- | -//- | 0.1 | 0.4 | 0.4 | 35 | ~8 | 13K geotherm - Diabase rheology lower crust - no subduction of incl. |
| IA_120_10_g13K | 120 | 10 | 1930 | -//- | -//- | -//- | -//- | -//- | -//- | 0.2 | 0.4 | 0.4 | 40 | ~8 | 13K geotherm - Diabase rheology lower crust - no subduction of incl. |
| IA_120_10_l10 | 120 | 10 | 1970 | 20 | -//- | -//- | -//- | -//- | -//- | 0.5 | 0.2 | 0.9 | 30 | ~11 | Diabase rheology lower crust - no subduction of incl. - upwards bending |

| | $W_{inc}$ [km] | $H_{inc}$ [km] | MP(x) [km] | MP(z) [km] | Shape | $\phi$ | E [kJ /mol] | $\rho$ [kg /m$^3$] | $Pl_{vel}$ [cm/a] | OP mean | OP exhume | OP max | OP % | exhume [Ma] | Comments |
|---|---|---|---|---|---|---|---|---|---|---|---|---|---|---|---|
| IW_reference | 150 | 10 | 1920 | 15 | elliptical | 36.9 | 445 | 3000 | 3 | 0.36 | 0.8 | 0.9 | 60 | ∼10 | complex bending of a large inclusion - L-shape |
| IA_120_10_hfa | 120 | 10 | 1970 | 20 | -//- | 45 | -//- | -//- | -//- | 0.3 | 0.4 | 0.9 | 30 | ∼10 | 9K geotherm - Diabase rheology lower crust - complex bending of a large inclusion - V-shape |
| IH_x1950 | 120 | 10 | 1950 | 20 | -//- | -//- | -//- | -//- | -//- | 0.4 | 0.6 | 0.6 | 100 | ∼10 | 11K geotherm - Diabase rheology lower crust - complex bending of a large inclusion - V-shape |
| IH_20_x1920 | 120 | 10 | 1920 | 20 | -//- | 45 | -//- | -//- | -//- | 0.6 | 1.1 | 1.1 | 60 | ∼13 | 11K geotherm - Diabase rheology lower crust - complex bending of a large inclusion - V-shape |
| IA_120_11_g9K_h3 | 120 | 11 | 1980 | 21 | -//- | -//- | -//- | -//- | -//- | 0.5 | 0.4 | >1.2 | 35 | ∼4 | Diabase rheology lower crust - 9K geotherm - V-shape |
| IA_120_11_g9K_h4 | 120 | 11 | 1980 | 21 | -//- | 55 | -//- | -//- | -//- | 0.5 | 0.4 | >1.2 | 35 | ∼5 | Diabase rheology lower crust - 9K geotherm - V-shape |
| IA_120_11_g10K_h | 120 | 11 | 1980 | 21 | -//- | 50 | -//- | -//- | -//- | 0.6 | 0.4 | >1.2 | 45 | ∼4 | Diabase rheology lower crust - 10K geotherm - V-shape |
| IA_120_11_g10K_h2 | 120 | 11 | 1980 | 21 | -//- | 55 | -//- | -//- | -//- | 0.6 | 0.4 | >1.2 | 35 | ∼4 | Diabase rheology lower crust - 10K geotherm - V-shape |
| IA_120_11_g9K_h | 120 | 11 | 1980 | 22 | -//- | 45 | -//- | -//- | -//- | 0.6 | 0.4 | >1.2 | 35 | ∼10 | 9K geotherm - Diabase rheology lower crust - V-shape |
| IA_120_11_g9K_h2 | 120 | 11 | 1980 | 22 | -//- | 50 | -//- | -//- | -//- | 0.6 | 0.4 | >1.2 | 35 | ∼10 | 9K geotherm - Diabase rheology lower crust - V-shape |
| IA_120_11_h | 120 | 12 | 1980 | 22 | -//- | 50 | -//- | -//- | -//- | 0.6 | 0.4 | >1.2 | 35 | ∼7 | Diabase rheology lower crust - V-shape |
| IA_120_11_h2 | 120 | 12 | 1980 | 22 | -//- | 55 | -//- | -//- | -//- | 0.6 | 0.4 | >1.2 | 35 | ∼7 | Diabase rheology lower crust - V-shape |
| IA_120_11_g10K_h2 | 120 | 11 | 1980 | 21 | -//- | 55 | -//- | -//- | -//- | 0.6 | 0.4 | >1.2 | 35 | ∼4 | 10K geotherm - Diabase rheology lower crust - V-shape |
| IA_120_12_h | 120 | 12 | 1970 | 22 | -//- | 45 | -//- | -//- | -//- | 0.35 | 0.4 | 0.8 | 30 | ∼12 | Diabase rheology lower crust - complex bending of a large inclusion - V-shape |
| IA_120_12_h2 | 120 | 12 | 1980 | 22 | -//- | 40 | -//- | -//- | -//- | 0.3 | 0.2 | 0.85 | 25 | ∼8 | Diabase rheology lower crust - complex bending of a large inclusion - V-shape |
| IA_120_12_h3 | 120 | 12 | 1980 | 22 | -//- | 30 | -//- | -//- | -//- | 0.25 | 0.1 | 0.7 | 25 | ∼7 | complex bending of a large inclusion - V-shape |
| IA_120_12_h5 | 120 | 12 | 1980 | 22 | -//- | 50 | -//- | -//- | -//- | 0.6 | 0.4 | >1.2 | 35 | ∼12 | Diabase rheology lower crust - V-shape - incl. completely subducts |
| IA_120_12_h6 | 120 | 12 | 1980 | 22 | -//- | 55 | -//- | -//- | -//- | 0.6 | 0.4 | >1.2 | 35 | ∼12 | Diabase rheology lower crust - V-shape - incl. completely subducts |

| | $W_{inc}$ [km] | $H_{inc}$ [km] | MP(x) [km] | MP(z) [km] | Shape | $\phi$ | E [kJ /mol] | $\rho$ [kg /m$^3$] | $Pl_{vel}$ [cm/a] | OP mean | OP exhume | OP max | OP % | exhume [Ma] | Comments |
|---|---|---|---|---|---|---|---|---|---|---|---|---|---|---|---|
| IW_reference | 150 | 10 | 1920 | 15 | elliptical | 36.9 | 445 | 3000 | 3 | 0.36 | 0.8 | 0.9 | 60 | ∼10 | complex bending of a large inclusion - L-shape |
| IA_120_12_g9K_h | 120 | 12 | 1980 | 21 | -//- | 50 | -//- | -//- | -//- | 0.6 | 0.4 | >1.2 | 35 | ∼9 | Diabase rheology lower crust - V-shape |
| IA_120_12_g10K_h | 120 | 12 | 1980 | 21 | -//- | 50 | -//- | -//- | -//- | 0.6 | 0.4 | >1.2 | 35 | ∼4 | 10K geotherm - Diabase rheology lower crust - V-shape |
| IA_120_12_l10_l | 120 | 12 | 1980 | 22 | -//- | 30 | -//- | -//- | -//- | 0.5 | 0.5 | >1.2 | 45 | ∼10 | Diabase rheology lower crust - V-shape - coesite field reached |
| IA_120_12_l10_LC | 120 | 12 | 1980 | 22 | -//- | 30 | -//- | -//- | -//- | 0.7 | - | 1 | 30 | no | Diabase rheology lower crust - $\phi_{LC}$ = 20 - V-shape - incl. completely subducts |
| Strong LC | 120 | 12 | 2000 | 22 | -//- | 30 | -//- | -//- | -//- | 0.4 | - | 0.9 | 50 | no | Diabase rheology lower crust - $\phi_{LC}$ = 30 - V-shape - incl. breaks |
| IA_120_12_l10_LC2 | 120 | 12 | 1980 | 22 | -//- | 30 | -//- | -//- | -//- | 0.8 | - | 1 | 30 | no | Diabase rheology lower crust - $\phi_{LC}$ = 20 - V-shape - incl. completely subducts |
| IA_120_12_l10 | 120 | 12 | 1980 | 22 | -//- | 40 | -//- | -//- | -//- | 0.5 | 0.5 | >1.2 | 40 | ∼7.4 | Diabase rheology lower crust - V-shape - coesite field reached |
| Strong inclusion | 120 | 12 | 2000 | 22 | -//- | 30 | -//- | -//- | -//- | 0.6 | 1.2 | >1.2 | 60 | ∼8 | V-shape - coesite field reached |
| IA_140_12 | 140 | 12 | -//- | 23 | -//- | -//- | -//- | -//- | -//- | 0.4 | - | 1 | 30 | no | 12K geotherm - Diabase rheology lower crust - L-shape - locking of subduction zone |
| IW_c_d15_cr1.5 | 200 | -//- | -//- | -//- | cuboid | 50 | -//- | -//- | 1.5 | 0.4 | - | 1.3 | 50 | no | locking of subduction zone |
| IW_e_200_10 | 200 | -//- | 2065 | -//- | -//- | -//- | -//- | -//- | -//- | 0.4 | - | 1 | 30 | no | fast subduction of incl. - almost no bending |
| IW_e_200_15 | 200 | 15 | -//- | -//- | -//- | -//- | -//- | -//- | -//- | 0.6 | 0.5 | 1.1 | 50 | ∼7 | fast complex bending of a huge inclusion - L-Shape |
| IW_e_200_20 | 200 | 20 | -//- | -//- | -//- | -//- | -//- | -//- | -//- | 0.6 | 0.5 | 1.1 | 50 | ∼12 | complex bending of a huge inclusion - L-Shape |

TABLE S2: Table of results of performed simulations. Reading from left to right: $W_{inc}$ [km]: width of the inclusion in km, $H_{inc}$ [km]: height of the inclusion in km, MP(x) [km]: midpoint of the inclusion in x direction in km, MP(z) [km] : midpoint of the inclusion in z in km Shape: shape of the inclusion (can be elliptical, cuboid or circular), $\phi$: friction angle used for the inclusion, E [kJ /mol]: activation energy used in the dislocation creep rheology for the inclusion, $\rho$ [kg /m$^3$]: density of the inclusion in kg/m$^3$, $Pl_{vel}$ [cm/a]: prescribed compression velocity of the plate in cm/a, OP mean: average overpressure observed in the whole inclusion in GPa, OP exhume: average exhumed overpressure of the inclusion, that was observed during the runtime of the simulation in GPa, OP max: average maximum overpressure observed in the inclusion in GPa, OP %: average percentage of overpressure with respect to the dynamic pressure, exhume [Ma]: approximated time after which the first part of the inclusion is exhumed to the surface, Comments: short description of either special parameters that where used, distinctive evolutional shape of the inclusion or special deformation patterns. The nomenclature for the simulations originates from a combination of the position of the inclusion in the domain (f.e. IA = (I)nclusion (A)bove the subduction channel), the x-y-position (f.e. 100_6_d1 = inclusion with a width of 100 km and a height of 6 km in a non-reference depth) and special additional cases (like a non-reference geotherm). Abbreviations: -//-: same value as the reference simulation, incl.: inclusion, WC: weak channel, LC: Lower crust